ANOMALOUS REFLECTION FROM PHASE GRADIENT METASURFACES FOR ARBITRARY INCIDENT ANGLES

by

Wihan Barnard

Submitted in partial fulfilment of the requirements for the degree
Master of Engineering (Electronic Engineering)

in the

Department of Electrical, Electronic and Computer Engineering
Faculty of Engineering, Built Environment and Information Technology

UNIVERSITY OF PRETORIA

January 2023

SUMMARY

ANOMALOUS REFLECTION FROM PHASE GRADIENT METASURFACES FOR ARBITRARY INCIDENT ANGLES

by

Wihan Barnard

Supervisor:	Prof. J. W. Odendaal
Co-supervisor:	Prof. J. Joubert
Department:	Electrical, Electronic and Computer Engineering
University:	University of Pretoria
Degree:	Master of Engineering (Electronic Engineering)
Keywords:	Artificial magnetic conductor (AMC), negative reflection, phase gradient metasurface (PGM), radar cross section (RCS)

Over the past few decades radar cross section (RCS) manipulation has become increasingly important. This increase in interest is due to the development and improvement of stealth technology. While many RCS manipulation techniques exist in the literature, most of these display certain shortcomings. The main disadvantages being complex target designs and narrow frequency bandwidth effectiveness. Metasurfaces are used to address these faults effectively for an array of practical applications. Checkerboard metasurfaces consists of an array of artificial magnetic conductor (AMC) elements, specifically two distinct AMC elements with phase differences of 180°. This causes phase cancellation between the AMC elements and redirects the scattered energy away from the angle of incidence. The other RCS manipulating metasurface is the phase gradient metasurface (PGM). This study will focus on predicting the reflected wave directions from PGMs with various phase gradients

for an arbitrary incident wave. The prediction of the reflected wave direction from PGMs are currently restricted to perpendicular incidence or small angles close to the normal vector.

The reflected wave directions from PGMs are determined in the literature by utilising the generalised Snell's law of reflection. This method is restricted by the relationship of the incident angle and phase gradient magnitude. If the critical value is exceeded the scattered wave direction becomes a complex value. Negative reflection was introduced to the adapted Snell's law to ensure the predicted reflected wave direction values remain real. However, it is shown that additional energy is also observed close to the plane of the PGM which is not predicted by any of the predicted modes. Array theory is used to determine the scan angle of an antenna array. The PGM can also be viewed as an antenna array where each AMC represents an antenna element with a magnitude and phase value. This study shows that the predicted scattered wave direction is accurately estimated by combining array theory concepts with the adapted Snell's law.

The proposed method of prediction is compared to a variety of simulated and measured metasurfaces. The reflected wave directions for a dual gradient metasurface with various incident angles are simulated in a computational electromagnetic (CEM) software package, CST Studio Suite, and compared to the proposed prediction method. A single gradient metasurface is designed at a different frequency and its bistatic and monostatic RCS is measured in the Compact Antenna Test Range (CATR) at the University of Pretoria.

LIST OF ABBREVIATIONS

AMC	artificial magnetic conductor
CATR	Compact Antenna Test Range
CEM	computational electromagnetic
EM	electromagnetic
EMC	electromagnetic compatibility
HPBW	half power beamwidth
PEC	perfect electric conductor
PGM	phase gradient metasurface
RAM	radar absorbing material
RCS	radar cross section

TABLE OF CONTENTS

LIST OF FIGURES

LIST OF TABLES

CHAPTER 1 INTRODUCTION

1.1 PROBLEM STATEMENT

1.1.1 Context of the problem

The echo area or radar cross section (RCS) is defined as "*the area intercepting the amount of power that, when scattered isotropically, produces at the receiver a density that is equal to the density scattered by the actual target*" [1]. The RCS of a target thus indicates its ability to reflect signals towards a receiver.

RCS manipulation has become increasingly important over the past half-century. This is due to the development and improvement of stealth technology. RCS reduction is achieved when the scattered energy towards the receiver is reduced. Traditionally RCS reduction is obtained by utilising radar absorbing materials (RAMs) and/or shaping of the object [2]. RAM is generally a lossy material which is used to transform the incident electromagnetic energy (EM) into heat energy which reduces the amount of reflected EM energy. The first example of such RAMs is the well known pyramidal foam absorbers usually found in electromagnetic compatibility (EMC) chambers. The physical, dimensional properties of these RAMs restrict their use to static, non-moving environments [3]. Other examples of RAM is radar absorbing coatings or screens such as the Salisbury screen [4], an ultra-thin RAM using lumped resistance, a Sievenpiper high impedance ground plane [5] and a perfect metamaterial absorber [6] creating multiple reflections to reduce the total backscatter and thus the RCS of the object. The advantages of these absorptive screens are convenience, flexibility and efficiency to the

detriment of the overall thickness [7]. Shaping aims to redirect the scattering energy of the target by altering its physical geometry. This increases the complexity of the target design. The disadvantage of RAMs is their effectiveness over only a narrow frequency bandwidth [8], while shaping can lead to complex and impractical designs.

Phase gradient metasurfaces (PGMs) are used to manipulate the RCS of planar structures for monostatic and bistatic RCS applications [9]. PGMs can be designed to reduce or enhance the RCS of structures for specific scenarios if it is possible to predict the direction of the reflected wave from the PGM for arbitrary incident angles. The anomalous reflected wave direction is determined from the incident wave vector component and additional phase gradient component of the PGM. Currently the direction of the scattered waves from PGMs with phase gradients in two orthogonal in-plane directions (dual gradients) are restricted to perpendicular incidence [10] or small incident angles close to the normal vector of the PGM [11], [12]. These restrictions are limiting the application of PGMs for RCS control to scenarios where the incident angle is smaller than the critical value [13]. This critical value occurs when the summations of the reflected wave vector, due to the incident angle, and the phase gradient vector becomes greater than the magnitude of the initial incident wave vector. A PGM was used in [14] to control the scattering direction of optical waves. In [10], [13] and [14] it is claimed that incident angles smaller than the critical value cause anomalous reflected waves and incident angles greater than the critical value cause non-radiating surface waves. In [15] it was shown that incident angles larger than the critical value are converted to evanescent surface waves. Negative reflection introduced in [15] for acoustic waves allowed for the prediction of reflected waves from a PGM for scenarios where the incident wave angle is greater than the critical value. This was done by incorporating diffraction order modes into the generalised Snell's law. This formulation still did not provide a complete estimation of all the reflected wave directions as shown by full wave simulations of a PGM in [16]. Additional energy was observed close to the plane of the PGM at $\theta_r = 90^\circ$ which was not predicted by any of the valid diffraction order modes. Following [3], [9], [17] and [18] the scattering from a PGM can be analysed as an equally spaced uniformly excited planar array. This method of analysis could possibly also be used to predict the reflected wave directions.

1.1.2 Research gap

From the context described above it is seen that the prediction of the direction of reflected wave directions for incident angles larger than the critical value has improved greatly. However, there is still additional energy observed in [16] which was not predicted by the current Snell's law method which incorporates the diffraction orders. A method is thus required to accurately predict all the reflected wave directions for an arbitrary incident angle from the scattering of a PGM with single or dual phase gradients.

1.2 RESEARCH OBJECTIVE AND QUESTIONS

The research questions this study will address are:

- Can the generalised Snell's law of reflection be extended, by incorporating diffraction order elements, to accurately predict the direction of reflected waves from a PGM with an arbitrary incident angle?
- Can this extended generalised Snell's law of reflection be further extended to account for phase gradients in multiple directions?
- Can the additional reflected energy close to the plane of the PGM, not predicted by the extended generalised Snell's law of reflection, be predicted?
- Can the reflected wave directions be measured and compared to the proposed method of prediction?

In [15] and [19] the direction of reflected waves from a PGM is calculated by incorporating diffraction order modes into the generalised Snell's law of reflection. This solution however only accounts for an incident wave in the same direction as the phase gradient. The first objective of this study is to extend the work of [15] and [19] to allow for an incident wave from an arbitrary angle. The second objective will aim to extend the method further to account for phase gradients in two orthogonal in-plane directions of the PGM.

Snell's law describes the relationship between the angle of incidence and reflection for a ray incident on a semi-infinite surface. Practical PGMs in the real world are finite structures and will not produce a uniform reflected plane wave, but rather a reflected wave with a finite beamwidth. The scattering from a PGM was analysed as an equally spaced uniformly excited planar array in [3], [17], [18] and [20]. The third objective of this study is to utilise array theory to account for the finite nature of PGMs to estimate the additional reflected energy observed close to the plane of the PGM.

The final objective will be to design, simulate and measure various PGMs which can be used to compare the reflected directions with the predicted directions.

1.3 APPROACH

To address a problem with partial solutions from different knowledge domains such as the problem posed in this study, a clear understanding of all the individual elements are required. First a literature study will be performed on various RCS manipulation techniques that use metasurfaces. Specific focus will be placed on the methods used to predict the reflected wave directions from these various types of metasurfaces. The basics of array theory will also be studied, specifically to analyse equally spaced uniformly excited planar arrays.

The proposed method to predict the reflected wave direction from [15] and [19] will be extended for an arbitrary incident wave and multiple phase gradients by expressing the existing equation in terms of the two in-plane directions of the PGM.

The next step will be to use array theory principles to analyse the bistatic scattering from a PGM. The diffraction order element must be incorporated into the array factor analysis. If done correctly the calculated direction of the peak of the scattered energy should provide the same direction as the Snell's law approach. Full wave bistatic simulations [16] of PGMs using CST Studio Suite showed additional reflected energy, close to the plane of the PGM at $\theta_r = 90°$, not predicted by any of the valid diffraction order modes. Array theory will be used

to illustrate why this scattered energy is observed but not predicted using Snell's law. The φ_r direction of the additional scattered energy (close to the plane of the PGM) will also be predicted using array theory.

Finally, the proposed method of prediction needs to be validated. Various PGMs will be designed with various phase gradients, designed at different frequencies, and simulated in CST Studio Suite [21]. A PGM will also be designed and manufactured. This PGM will be measured in the compact antenna test range (CATR) of the University of Pretoria. Monostatic RCS measurements will be conducted and compared to simulated results while validating the reflected wave directions with the proposed method. The CATR will also be reconfigured to conduct bistatic RCS measurements which will again be compared to simulated results while validating the reflected wave directions with the proposed method.

1.4 RESEARCH GOALS

The first research goal of this study is to extend the generalised Snell's law of reflection from [15] and [19] to account for an incident wave from an arbitrary angle. The second goal is to further extend the prediction method to incorporate phase gradients in the two orthogonal in-plane directions of the PGM. The third goal is to provide a method to predict the additional scattered energy not predicted by the extended Snell's law. The fourth goal is to design, simulate and measure PGMs which can be used to validate the prediction methods proposed.

1.5 RESEARCH CONTRIBUTION

In this dissertation the generalised Snell's law of reflection used by [15] and [19] is extended to account for arbitrary incident angles. The prediction method is then extended further to account for phase gradients in the two orthogonal in-plane directions of the PGM. Array theory is utilised to show why certain diffraction orders do not predict a reflected wave, even though significant scattered energy is observed in the simulated results. The unpredicted

observed scattered energy is attributed to the finite nature of practical PGMs in the real world whose scattering produces reflected waves with a finite beamwidth and not uniform reflected plane waves. The prediction methods from this study are then validated by comparing the estimated directions of the reflected waves from planar PGMs with simulated and measured monostatic and bistatic RCS results.

1.6 RESEARCH OUTPUTS

- W. Barnard, J. W. Odendaal and J. Joubert, "Predicting the direction of the reflected wave from a phase gradient metasurface with arbitrary incident angle", in *2021 IEEE International Symposium on Antennas and Propagation and USNC-URSI Radio Science Meeting*, Singapore, 2021.
- W. Barnard, J. W. Odendaal and J. Joubert, "Anomalous Reflection from a Phase Gradient Metasurface with Arbitrary Incident Angle", submitted to *IEEE Access*, October 2022.

1.7 OVERVIEW OF STUDY

Chapter 1 provides the context for the research problem of the study. How the problem was approached, the research objective of the study and contributions of the study is also discussed. Chapter 2 discusses the current literature concerning RCS manipulation techniques with metasurfaces. The method of scattered wave prediction for these metasurfaces is also discussed.

In Chapter 3 the existing theory to predict the direction of the reflected waves is extended for arbitrary incident angles. The method is further improved by accounting for orthogonal phase gradients. Array theory was used to determine if significant scattered energy shifts into the visible space for a given diffraction order. The simulation environment and the design of a PGM for simulations, including the design and combination of the artificial magnetic

conductor (AMC) elements to form the PGM, is also discussed in this chapter. Lastly, the proposed prediction method presented in this chapter is validated by comparing calculated results to various simulated results. The PGMs in this chapter include single phase gradients, orthogonal phase gradients and a multitude of incident angles.

Chapter 4 presents the measured results for various PGMs. The design of the manufactured PGM is discussed as well as the measurement setups in the CATR for monostatic and bistatic measurements. This chapter is also used to validate the simulated results and proposed prediction method presented in Chapter 3.

Lastly, the study is concluded in Chapter 5. The contributions of the study are highlighted and some suggestions for future work on this topic are discussed. Addendum A contains additional simulated results and information used to accurately predict the reflected wave directions for each relevant scenario, as shown in Chapter 3. Addendum B contains the software code used for calculations and validation.

CHAPTER 2 LITERATURE STUDY

2.1 CHAPTER OVERVIEW

This chapter presents the literature study for this dissertation. A broad overview of traditional and modern RCS manipulation techniques is discussed in Section 2.2. The two most promising techniques for RCS manipulation using metasurfaces are highlighted in Sections 2.3 and 2.4. The various uses of these metasurfaces presented in the literature is also discussed. The importance of the contribution of this study is highlighted in Section 2.4.2 which shows the evolution of the scattered wave direction prediction methods from a PGM. Each prediction method improves on the previous, but not without their own shortcomings. The research gap is also illustrated in Section 2.4.2 by showing the limitations of the current scattered wave direction prediction methods.

2.2 RCS MANIPULATION TECHNIQUES

Traditional RCS manipulation techniques include using RAMs and/or shaping of objects to reduce the scattered energy towards the received [2]. The usage of RAMs are limited to static and non-moving environments [3]. RAM coatings or screens, such as the Salisbury screen [4], create multiple reflections which reduce backscatter. These absorptive screens are convenient, flexible and efficient with the drawback of increasing overall thickness [7]. RAMs are however only effective over a narrow frequency bandwidth [8]. Lastly, shaping

redirects the scattering energy of the target by altering its physical geometry which can lead to complex and impractical designs.

Redirection of the scattered energy using metasurfaces is an alternative RCS reduction technique which has become increasingly popular in recent years [22]. These metasurfaces consist of a planar array of resonant unit cells mounted on a dielectric substrate. The unit cells can be designed to manipulate most basic properties of electromagnetic waves. Two popular redirection methods include the use of checkerboard metasurfaces and also PGMs. Both these designs make use of AMC elements. Electromagnetic bandgap (EBG) materials are artificially engineered materials that prevent the propagation of electromagnetic waves at certain frequency bands. An important characteristic of EBG materials is that their phase reflection coefficient varies between -180° and $+180^\circ$. When the phase reflection falls between -90° and $+90^\circ$ it is referred to as an AMC [7]. AMC elements were first proposed in 1999 [23] and have since become widely utilised in antenna and electromagnetic applications. The phase of the reflection coefficient of these AMC elements can be controlled by varying different parameters of the element design [24].

2.3 CHECKERBOARD METASURFACE

The checkerboard metasurface owes its name to the specific arrangement of two different subcells, each consisting of an AMC specifically designed the have a specific phase reflection at a desired frequency. The two AMC elements are designed with phase reflections that are 180° out of phase of each other over the desired frequency band. This causes destructive interference which leads to the scattered energy being directed away from the normal plane of incidence. Examples of these metasurfaces are found in [3], [7], [17], [18], [22], [25], [26], [27], [28], [29], [30], [31], [32], [33], [34] and shown in Figure 2.1. Traditionally two subcells are configured in the checkerboard arrangement with each subcell consisting of an equal amount of single AMC elements. When correctly designed these metasurfaces redirect the scattered EM fields effectively away from the specular direction. When a perfect electric conductor (PEC) surface is illuminated by a plane wave, most of the scattered energy will be

directed back towards the specular direction as shown in Figure 2.2. When the same plane wave illuminates the checkerboard metasurface, the reflection phase for each of these subcells are 180° out of phase and results in destructive interference. For a generic representation of a checkerboard metasurface the scattered waves are then redirected along the four quadrants with four major lobes as shown in Figure 2.3 [8].

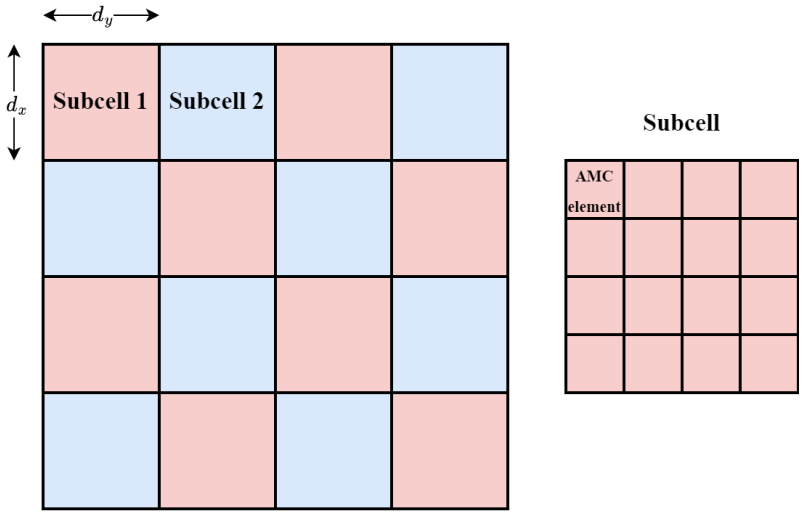

Figure 2.1. A generic design of a checkerboard metasurface showing the arrangement of subcells to form the surface as well as the layout of a subcell which consists of AMC elements.

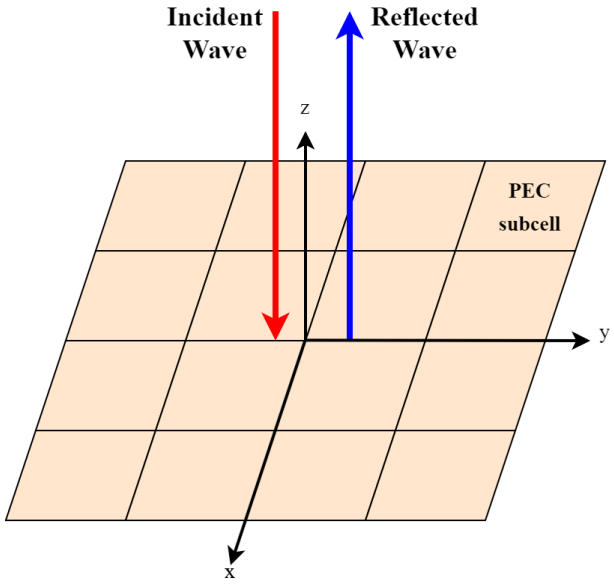

Figure 2.2. Simulated bistatic RCS for a PEC surface indicating reflected wave scattering direction.

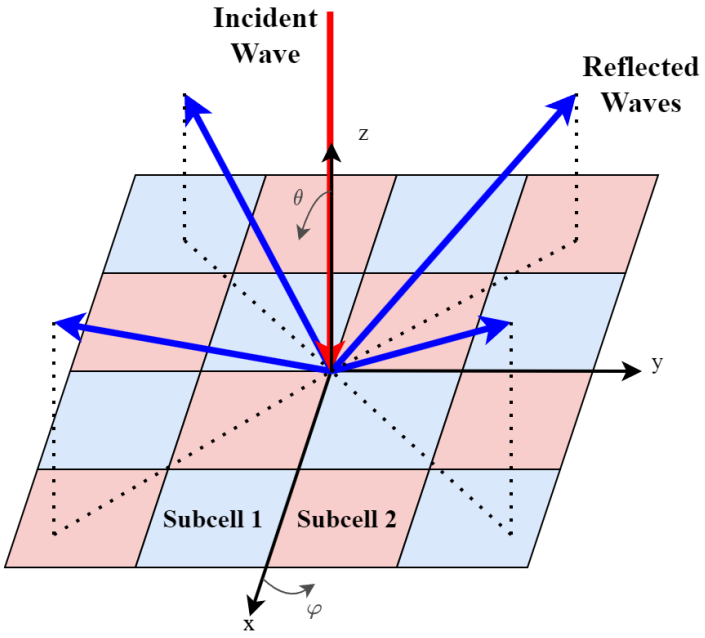

Figure 2.3. Simulated bistatic RCS for a checkerboard metasurface indicating the scattering directions of the reflected waves due to the out of phase subcells.

Following [3], [17], [18] and [20] the scattering from the PGM can be analysed as an equally spaced uniformly excited planar array. Using array theory the direction of the reflected waves can be estimated as [8],

$$tan\varphi_{m,n} = \frac{sin\theta_i sin\varphi_i \pm (2n+1)\frac{\delta\phi_y}{\beta d_y}}{sin\theta_i cos\varphi_i \pm (2m+1)\frac{\delta\phi_x}{\beta d_x}}$$

$$sin^2\theta_{m,n} = [sin\theta_i sin\varphi_i \pm (2n+1)\frac{\delta\phi_y}{\beta d_y}]^2 + [sin\theta_i cos\varphi_i \pm (2m+1)\frac{\delta\phi_x}{\beta d_x}]^2, \quad (2.1)$$

where $(\theta_{mn}, \varphi_{mn})$ indicate the direction of the reflected waves, (θ_i, φ_i) the incident angle, $\delta\phi_x$ and $\delta\phi_y$ are the phase differences between the adjacent AMC elements in the x- and y-direction, respectively. Here d_x and d_y are the distances between the adjacent subcells and β is the wave number/phase constant of the incident wave. The directions of the four major reflected lobes are estimated, using (2.1) with $m = n = 0$.

An analytical expression to calculate the RCS reduction for these checkerboard metasurfaces is presented in [7] and [35] as,

$$RCS\ Reduction = |\frac{A_1 e^{j\phi_1} + A_2 e^{j\phi_2}}{2}|^2, \tag{2.2}$$

where ϕ_1 and ϕ_2 are the phases of the reflected fields reflected by AMC 1 and AMC 2, while A_1 and A_2 are the reflection coefficient amplitudes of the AMC elements [7]. Equation (2.2) can be used to calculate that a phase difference of $(180 \pm 37)^\circ$ is needed to reduce the RCS by at least 10 dB.

One of the first successful implementations of these checkerboard metasurfaces showing significant RCS reduction is found in [3]. The surface presented consists of a combination of PEC and AMC cells in the traditional checkerboard configuration as shown in Figure 2.1. The AMC used is a Sievenpiper [23] mushroom structure. The RCS reduction of the checkerboard metasurface, when compared to a similar sized PEC surface, is about 5%. It is clear that the operating bandwidth of these checkerboard metasurfaces is primarily dependent on the design of the AMC elements.

In [18] and [25] the PEC used in [3] was replaced with a second AMC element. Two square patches of different sizes were selected, predicting a working frequency band of 55% and an actual realised 10 dB reduction band of 25%. The same concept was used in [18], but instead of simple patch elements a more complicated Jerusalem Cross AMC element was implemented. The benefit of the Jerusalem Cross is that the different sized crosses have a more stable phase reflection transition region, meaning that the two AMC elements are out of phase by 180° for a larger frequency band. A 40% RCS reduction is realised using these Jerusalem Cross AMC elements.

A square and circular patch was used as the AMC elements in [7] to improve the 10 dB RCS reduction band to 60%. The AMC elements were also arranged in a hexagonal checkerboard layout which provided the same RCS reduction bandwidth, with the added benefit of creating six (instead of four) reflected lobes which lead to a further reduction in the bistatic RCS of the

metasurface. The use of single band and dual band AMC elements, in contrast to two single band AMC elements, improved the 10 dB RCS reduction band to 83% [17]. The dual band AMC element is created by using the square patch AMC from [7] and adding an outer ring. It is suggested to first optimise the surface using two single band AMC elements and only then converting one of the AMC elements to a dual band AMC element to achieve a wider RCS reduction bandwidth. A dual band AMC element resonates at two different frequencies. In [26] and [27] two dual band AMC elements were used to design a checkerboard metasurface realising 10 dB RCS reduction bandwidths of 61% (3.94-7.4 GHz) and 24% (8.41-10.72 GHz) respectively. A checkerboard metasurface was even implemented on a flexible cylindrically curved ground plane [36]. Two different radii of curvature were evaluated and a 5 dB RCS reduction frequency bandwidth of 22-25% was realised for HH and VV polarisations. The AMC elements used to design the flexible metasurface consisted of a simple patch and circular AMC element.

The arrangement of the AMC elements, e.g. the number of AMC elements per subcell, spacing between AMC elements and number of subcells on the metasurface, plays an important role in the efficiency of the metasurface. A checkerboard metasurface with an RCS reduction bandwidth of 3% was improved to have an RCS reduction bandwidth of 42.3% by using a genetic optimisation algorithm to determine the optimal arrangement of the AMC elements [30]. In [29] a simple square patch and square ring AMC element was also arranged in a non-traditional 3×10 square lattice to increase the amount of reflected sidelobes and thus reducing the amount of reflected fields towards the monostatic received. The concept of a coding metasurface was introduced in [32]. This is where a certain bit value is assigned to a subcell of AMC elements. In contrast to the existing checkerboard metasurfaces this surface is designed by implementing various coding sequences of the subcells of AMC elements to achieve a desired dispersion. Another coding metasurface was presented in [31] and was designed to behave like an RCS reducing checkerboard metasurface outside of a certain operating frequency band while acting like a mirror with a specular reflection property within the band.

2.4 PHASE GRADIENT METASURFACE

A PGM consists of AMC elements with regular inter-element phase variation. The metasurface can be used to control the reflected wave directions by additional wave vectors to redirect the reflected or refracted wave towards a desired direction [24]. A generic design of a PGM subcell with a regular phase variation of $\delta\phi = \frac{2\pi}{3}$ rad is shown in Figure 2.4. This figure shows 3×3 AMC elements which together form one subcell of a PGM. The reflected wave will scan in the direction of the phase lagging element [37]. The phase gradient vector direction is thus also in the direction of the phase lagging element. In Figure 2.4 the lagging element is in the negative *y*-axis direction meaning the phase gradient vector will also be in this direction.

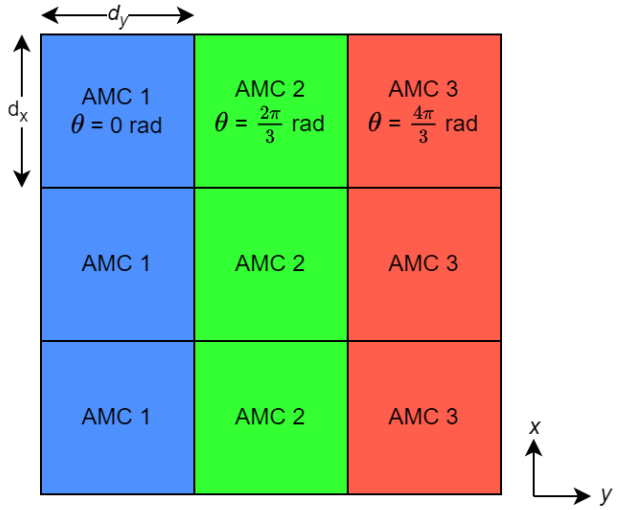

Figure 2.4. A generic design of a PGM subcell, consisting of 3×3 AMC elements, with regular inter-element phase variation.

2.4.1 RCS manipulation using PGMs

A PGM was originally used to control light by producing a spiral wave [14]. Due to the phase variation on the surface of the PGM, the classic Snell's Law of reflection (angle of incidence is equal to angle of reflection), will not be suitable to calculate the angle of reflection any more [10]. Examples of these PGMs are found in [10], [11], [12], [14], [24], [38], [39], [40], [41], [42], [43].

The RCS of a dihedral corner was reduced using a strip grating technique [38], which was implemented by loading a corner reflector with conducting strips periodically on a dielectric sheet. A reduction of 20-30 dB was obtained for the TE polarisation. PGMs have also been used to control the main beam angle of a microstrip antenna [39]. Different reflected wave directions were produced for different phase differences on the PGM. The 10 dB reduction was shown to have a bandwidth of 1.3%, but the main contribution made in [39] was showing that the theoretical, simulated and measured results of the main beam angle calculation conformed, proving the design method from [39] as a viable design method.

Elliptical rings were used as AMC elements to form a PGM with a phase gradient in the y-axis direction [41]. The single phase gradient displayed great efficiency for anomalous reflection. This anomalous reflection scattered the reflected wave away from the incident angle leading to effective monostatic RCS reduction. The performance of the PGM degrades as the incident angle moves away from the normal plane of incidence. The PGM was shown to be effective between the incident angles of 0° and 40° for the surface in [41]. This PGM was then applied to the inside of a cube cavity and resulted in a 5 dB RCS reduction for incident angles between 0° and 30°. Another PGM with a single phase gradient was presented in [12] showing 10 dB monostatic RCS reduction from 7.8-17 GHz (74.19% bandwidth).

In [10] and [40] a PGM was presented which displayed significant RCS reduction of a slot array antenna. The AMC elements used for this PGM consisted of a combination of cross and square ring patches. The size of these patches were varied to produce a phase difference of 90° between the four adjacent AMC elements. The 10 dB monostatic RCS reduction bandwidth under normal incidence was shown to be 78%. The arrangement of the subcells from [10] was varied in [40] to enhance the bistatic RCS reduction without compromising the monostatic RCS reduction bandwidth. In [44] a PGM is proposed based on the random distribution of AMC elements which reduced the RCS of the surface by 40 dB for fractional bandwidth of 50 %. In [11] a phase gradient consisting of 8 AMC elements is presented. The PGM was arranged in a spiral pattern and ultrabroadband RCS reduction was achieved (63%). The arrangement also ensured the surface was polarisation independent and less sensitive to the incident angle while the design was kept simple without any arrangement optimisation

needed. In [45] a PGM is proposed which shows significant RCS reduction while enhancing the gain of a conventional patch antenna.

2.4.2 Predicting the reflected wave directions

PGMs can be used to manipulate the RCS of planar structures for both monostatic and bistatic RCS applications [9]. If the direction of the reflected waves from a PGM can be predicted, then the PGM can be used to either reduce or enhance the RCS of a structure in a specific direction as shown in [46]. The PGM presented in [10] for wideband RCS reduction of a slot array antenna only considered normal incidence ($\theta_i = 0$). The one dimensional generalised Snell's law of refraction was used to predict the reflected angle θ_r as [14], [24], [39], [41],

$$sin\theta_r - sin\theta_i = \frac{\nabla\phi}{\beta_i}, \tag{2.3}$$

where β_i is the magnitude of the wave vector of the incident wave and $\nabla\phi$ is the magnitude of phase gradient. The phase gradient is described as the phase variation of the AMC element ($\delta\phi$) over the distance between AMC elements (d), $\nabla\phi = \frac{\delta\phi}{d}$. Equation (2.3) is visually represented in Figure 2.5 illustrating a reflective PGM with the incident angle and phase gradient in a single axis direction.

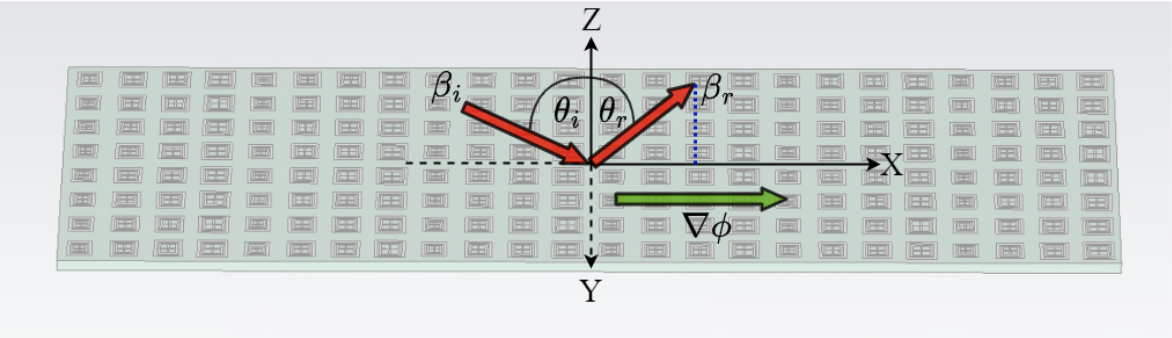

Figure 2.5. A reflective PGM with a phase gradient and incident wave in a single axis direction, illustrating the incident and reflected wave vectors as well as phase gradient vectors.

In [10], [11], [12] (2.3) was extended to account for phase gradients in two orthogonal in-plane directions. The direction of the reflected wave, θ_r and φ_r, is given as,

$$\theta_r = \arcsin\left(\frac{\sqrt{(\nabla\phi_x + \beta_{ix})^2 + (\nabla\phi_y + \beta_{iy})^2}}{\beta_i}\right) \tag{2.4}$$

$$\varphi_r = \arctan\left(\frac{\beta_{iy} + \nabla\phi_y}{\beta_{ix} + \nabla\phi_x}\right). \tag{2.5}$$

The $\nabla\phi_x$ and $\nabla\phi_y$ terms describe the orthogonal phase gradients of the PGM along the x- and y-axis and the β_{ix} and β_{iy} terms are the magnitudes of the in-plane wave vector components of β_i. In Figure 2.6 a reflective PGM which consists of 3×3 subcells and 4×4 AMC elements per subcell is shown. This figure also illustrates the terms described in (2.4) and (2.5).

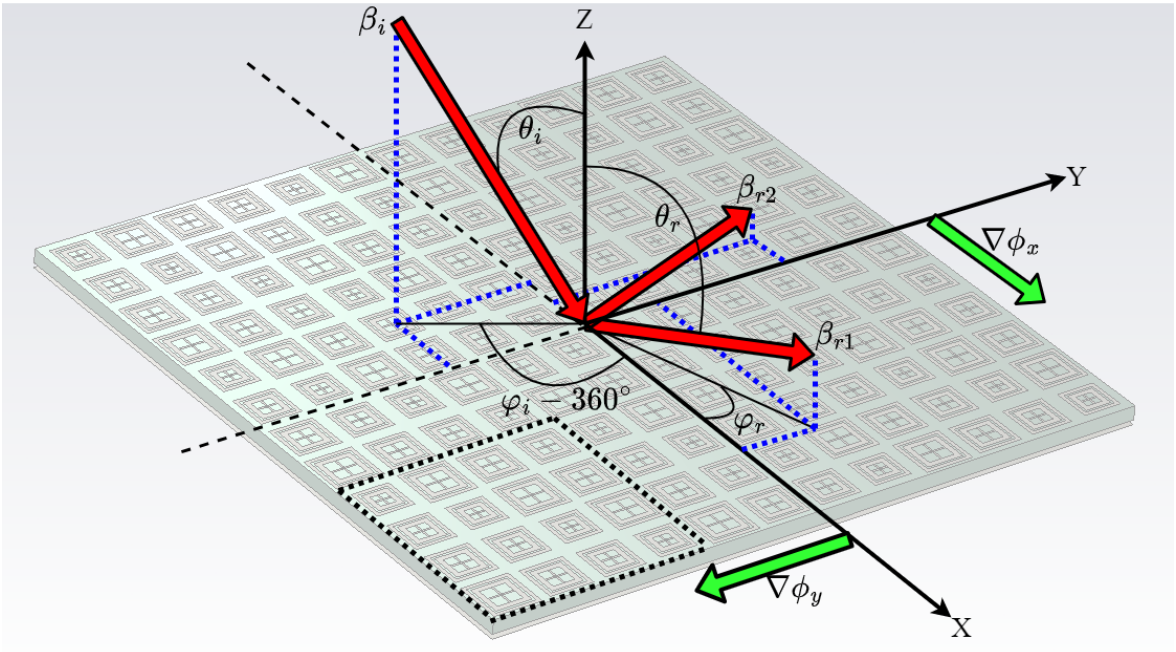

Figure 2.6. A reflective PGM with phase gradients in two orthogonal in-plane directions, illustrating the incident and reflected wave vectors as well as phase gradient vectors. The dashed square indicates a subcell consisting of 4x4 AMC elements.

In [10], [13], [14] and [47] it is stated that a PGM will either anomalously reflect or couple an incident wave into a surface wave. The critical value determining this threshold is described as the angle of incidence above which the reflected wave is no longer anomalously reflected,

but coupled into a surface wave [14]. In particular, considering (2.4), if the incident angle exceeds the critical value, the numerator will be larger than the denominator and θ_r will result in in a complex value. When this occurs [12] states the incident wave is coupled into a surface wave and the in-plane direction of this surface wave, φ_r, can be calculated from (2.5).

Negative reflection was introduced in [15] for acoustic waves with incident angles larger than the critical value. It was shown that not all the energy is necessarily coupled into surface waves when the incident angle is larger than the critical value and reflected waves of significant magnitudes were observed at other angles. The generalised Snell's law of reflection becomes wave vector dependent and is reformulated as follows [15], [19],

$$sin\theta_r - sin\theta_i = \frac{1}{\beta_i}(\xi + \eta_G G), \tag{2.6}$$

where $\xi = \sigma(\frac{2\pi}{\rho_s})$ represents the phase gradient term, ρ_s is the subcell's period, $\sigma = 1$ or $\sigma = -1$ indicates the direction of the phase gradient, $G = \frac{2\pi}{\rho_s}$ is the amplitude of the reciprocal lattice vector and η_G is the diffraction order.

The inclusion of the diffraction order element, η_G, in (2.6) ensures the validity of the equation, especially if the incident wave angle exceeds the critical value. In [19] multiple reflected modes were estimated for all valid values of η_G. However, in [16] full wave scattering simulations of PGMs using CST Studio Suite [21] show additional scattered energy close to the plane of the PGM which was not estimated by any valid values of η_G (non-local modes) with (2.6). In [48] a general method was proposed to control the diffraction pattern both in angle and energy ratio between the scattered beams. This proposed method does however not account for scattered beams which peaks would fall outside but close to the plane of the PGM.

2.5 SUMMARY

This chapter discusses why metasurfaces are of great interest for RCS manipulation in the modern era. RCS reduction utilising checkerboard metasurfaces is shown. The prediction

of the reflected wave directions for checkerboard metasurfaces can be estimated using the phase cancellation principle, type of AMC elements used and the layout of the metasurfaces. Thereafter PGMs are investigated and their use in the manipulation of the RCS of planar objects. If the reflected wave directions of a PGM can be estimated, the PGM can be designed for RCS reduction or enhancement. The methods used in the literature to predict the reflected wave direction from a PGM are discussed and the limitations and reasons for these limitations are discussed.

CHAPTER 3 PREDICTING REFLECTED WAVE DIRECTIONS OF A PGM

3.1 CHAPTER OVERVIEW

This chapter develops a method to predict the reflected wave directions from a PGM with orthogonal phase gradients and arbitrary angle of incidence. Section 3.2 formulates the problem this study aims to address. The generalised Snell's law of reflection, which includes a diffraction order, is extended to account for arbitrary incidence and orthogonal phase gradients in Section 3.3. The formulation provided in Section 3.3 to predict the direction of the reflected wave is derived using antenna array theory principles in Section 3.4 reinforcing the statements made in [20] and [17] that PGMs can be analysed as planar arrays. Section 3.4 also illustrates why certain diffraction orders predict no reflected wave directions, but scattered energy for this mode is clearly observed. The simulation environment setup and design of a PGM for simulation is discussed in Section 3.5.

In Section 3.6 the simulated bistatic RCS of a PGM with phase gradients in two orthogonal in-plane directions with an incident angle of $\theta_i = 60°$, $\varphi_i = 20°$ is given. The proposed prediction method is applied to the specific simulations and compared to the simulated results. Additional simulations were conducted and the results are summarised in Table 3.6 in Section 3.6.3. Lastly, Section 3.6.4 discusses the validity of the proposed method for all incident angles, not

only angles above the critical value.

3.2 PROBLEM FORMULATION

Figure 3.1 shows a reflective PGM consisting of 3×3 subcells and 4×4 AMC elements per subcell, realising phase gradients in the two orthogonal in-plane directions of the PGM. The problem this study aims to address is: given a PGM (such as the one in Figure 3.1) with a known incident wave direction, θ_i and φ_i, what will the reflected wave direction, θ_r and φ_r be?

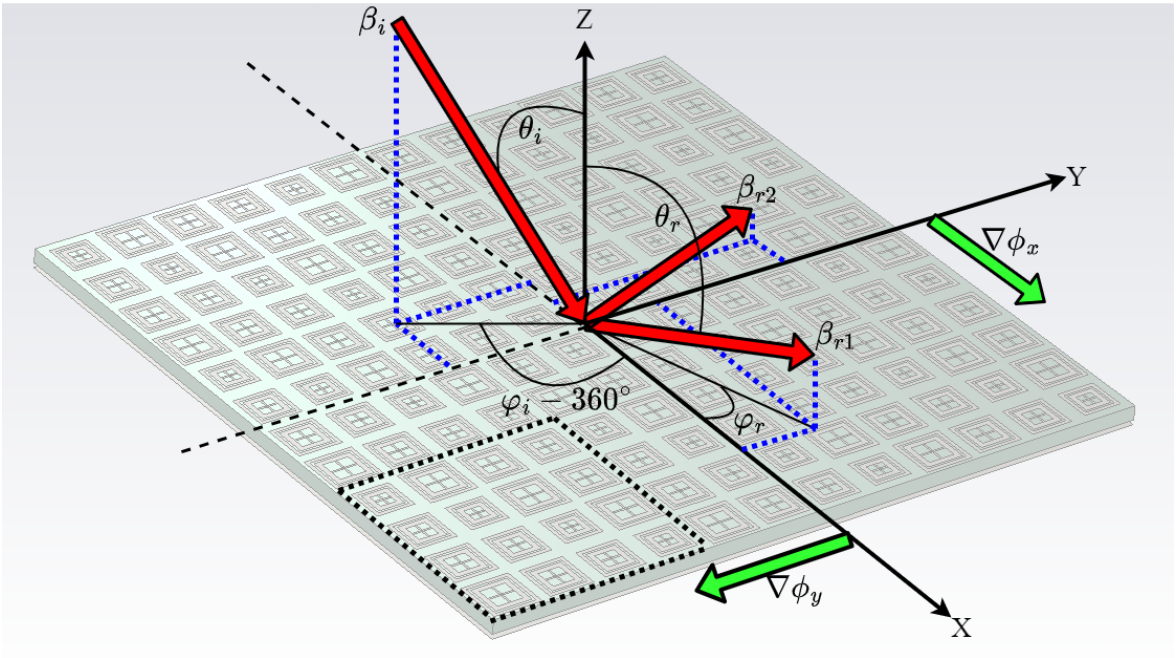

Figure 3.1. A reflective PGM with phase gradients in two orthogonal in-plane directions, illustrating the incident and reflected wave vectors as well as phase gradient vectors. The dashed square indicates a subcell consisting of 4×4 AMC elements.

Predicting the direction of the scattered waves from PGMs with dual gradients is currently restricted to perpendicular incidence [10] or small incident angles close to the normal vector [11], [49]. These restrictions are limiting the application of PGMs for RCS control to scenarios where the incident angle is smaller than the critical value [13], e.g., when the summation of

the reflected wave vector due to the incident angle and the phase gradient vector does not exceed the magnitude of the initial incident wave vector. Additionally, these methods only estimate a single reflected wave direction and do not account for multiple active modes.

Snell's law of reflection, (2.4) and (2.5), predicts the reflected wave direction [10], [11], [14], [49] for incident angles less than the critical value. [10], [13] and [14] claim incident angles less than the critical value cause anomalous reflected waves while incident angles exceeding the critical value lead to surface wave reflection. In [15], not all incident angles exceeding the critical value lead to surface wave reflections. Incident angles exceeding the critical value for acoustic waves illustrate the phenomenon of negative reflection [15]. A diffraction order element, η_G, was introduced into Snell's law (2.6) in [15], which makes it possible to predict the reflected direction from a PGM for scenarios where the incident wave angle is larger than the critical value. Subsequently, [19] considered the bistatic RCS of a PGM with a one-dimensional phase gradient and estimated multiple directions for reflected modes. However, full wave scattering simulations of PGMs using CST Studio Suite [9] show additional reflected energy, close to the plane of the PGM at $\theta_r = 90°$, not predicted by any of the valid diffraction order modes.

The generalised Snell's law of refraction/reflection from [15] and [19] will be extended to account for PGMs with different phase gradients in two orthogonal in-plane directions. Additionally a method will be developed to predict the reflected energy close to the plane of the PGM, which was not predicted by the extended Snell's law using the diffraction orders.

3.3 GENERALISED SNELL'S LAW OF REFLECTION

In [15] the concept of negative reflection was introduced for acoustic waves with incident angles producing imaginary reflected wave directions. This causes the generalised Snell's law of reflection to become wave vector dependent. Snell's law was then reformulated, as shown in (2.6), to account for the negative reflection by including a diffraction order element [15], [19]. In (2.6) only a one-dimensional phase gradient is considered along with an incident angle

in the same direction as the phase gradient. Equation (2.6) can be rewritten and simplified as,

$$\beta sin\theta_r = \beta sin\theta_i + \sigma\nabla\phi(1+\eta_G), \tag{3.1}$$

where $\nabla\phi$ is the phase gradient and σ the direction of the phase gradient.

Extending (3.1) to account for an incident wave from an arbitrary direction (θ_i, φ_i) and for dual phase gradients in the x- and y-directions ($\nabla\phi_x$, $\nabla\phi_y$), results in,

$$\beta sin\theta_r cos\varphi_r = \beta sin\theta_i cos(\varphi_i - \pi) + \sigma\nabla\phi_x(1+\eta_G) \tag{3.2}$$

$$\beta sin\theta_r sin\varphi_r = \beta sin\theta_i sin(\varphi_i - \pi) + \sigma\nabla\phi_y(1+\eta_G). \tag{3.3}$$

The reflected wave directions (θ_r, φ_r) are determined by simultaneously solving (3.2) and (3.3) for different diffraction order values, η_G.

3.4 ANTENNA ARRAY THEORY AND SCATTERING FROM A PGM

In [19] multiple directions for reflected modes were estimated for all valid values of η_G. Full wave scattering simulations [16] of PGMs using CST Studio Suite shows additional reflected energy, close to the plane of the PGMs at $\theta_r = 90°$, not predicted by any of the valid diffraction order modes.

Snell's law describes the relationship between the angle of incidence and reflection for a ray incident on a semi-infinite surface. Practical PGMs in the real world are finite as illustrated in Figure 2.6. A PGM of finite size will not produce a uniform reflected plane wave, but rather a reflected wave with a finite beamwidth.

A PGM is designed using AMC elements which provide a uniform amplitude reflection and varied phase reflection. This phase reflection is controlled by varying certain parameters of the AMC elements [10]. Figure 3.1 shows a reflective PGM consisting of 3×3 subcells and 4×4

AMC elements per subcell, realising phase gradients in two orthogonal in-plane directions of the PGM.

Following [3], [17] and [18] the scattering from the PGM can be analysed as an equally spaced uniformly excited planar array. The array factor is described as the pattern of an array with actual elements replaced by isotropic point sources [37]. The normalised array factor for uniformly excited and equally spaced linear arrays given in [37] is,

$$f(\psi) = \frac{sin(N\psi/2)}{Nsin(\psi/2)}, \tag{3.4}$$

where N represents the number of elements in the uniformly excited, equally spaced linear array and ψ the resulting inter element phase difference is,

$$\psi = \beta d\, cos\theta + \alpha. \tag{3.5}$$

β is known as the wave number or phase constant and calculated as,

$$\beta = \frac{2\pi}{\lambda}, \tag{3.6}$$

and d is the uniform spacing between adjacent elements and α the phase difference between elements.

Main beam scanning is achieved by controlling the phase of the transmitting antenna elements [37]. From (3.4), $f(\psi)$ is maximum when $\psi = 0$ [50]. The desired scan angle, θ_0, is then explicitly incorporated into ψ as,

$$\psi = \beta d\, (cos\theta - cos\theta_0) + \alpha. \tag{3.7}$$

The scattering from a PGM is incorporated into (3.7) by equating the phase gradient between elements, $\nabla\phi d$, to the phase difference, α; the desired scan angle, θ_0, to the specular reflected angle due to the angle of incidence, $-\theta_i$ and also including the diffraction order, η_G, from

[15] and [19] as,

$$\psi = \beta d\ (cos\theta - cos\theta_0) - \nabla\phi d(1+\eta_G). \tag{3.8}$$

The normalised array factor for uniformly excited and equally spaced planar arrays adapted to the scattering from a PGM for an incident wave from an arbitrary direction with dual phase gradients in the x- and y-directions ($\nabla\phi_x$, $\nabla\phi_y$) is,

$$f(\psi_x, \psi_y) = |\frac{sin(\frac{N_x\psi_x}{2})}{N_x sin(\frac{\psi_x}{2})} \times \frac{sin(\frac{N_y\psi_y}{2})}{N_y sin(\frac{\psi_y}{2})}|, \tag{3.9}$$

with inter element phase difference,

$$\psi_x(\theta,\varphi) = \beta d_x(sin\theta cos\varphi - sin\theta_i cos(\varphi_i - \pi)) - \nabla\phi_x d_x(1+\eta_G) \tag{3.10}$$

$$\psi_y(\theta,\varphi) = \beta d_y(sin\theta sin\varphi - sin\theta_i sin(\varphi_i - \pi)) - \nabla\phi_y d_y(1+\eta_G), \tag{3.11}$$

in the x- and y-direction, respectively. (N_x, N_y) represents the number of AMC elements in one subcell and (d_x, d_y) the spacing between the centre points of the AMC elements in the x- and y-direction, respectively.

The normalised array factor, $f(\psi_x, \psi_y)$, for a subcell with 4×4 AMC elements plotted as a function of the inter element phase difference, is shown in Figure 3.2. The visible space regions for different diffraction orders, η_G, are represented by the ellipses labelled A, B, C and D for diffraction values, $\eta_G = 0, -1, -2$ and -3, respectively. The visible space regions for different diffraction orders, η_G, are calculated [37] as,

$$\psi_x(0,0) - \beta d_x < \psi_x < \psi_x(0,0) + \beta d_x \tag{3.12}$$

$$\psi_y(0,0) - \beta d_y < \psi_y < \psi_y(0,0) + \beta d_y. \tag{3.13}$$

The visible space region is better described by the equation of an ellipse as,

$$\frac{(\psi_x - \psi_x(0,0))^2}{(\beta d_x)^2} - \frac{(\psi_y - \psi_y(0,0))^2}{(\beta d_y)^2} = 1, \tag{3.14}$$

where $(\psi_x(0,0),\ \psi_y(0,0))$ is the centre of the ellipse, βd_x the x-axis radius and βd_y the y-axis radius.

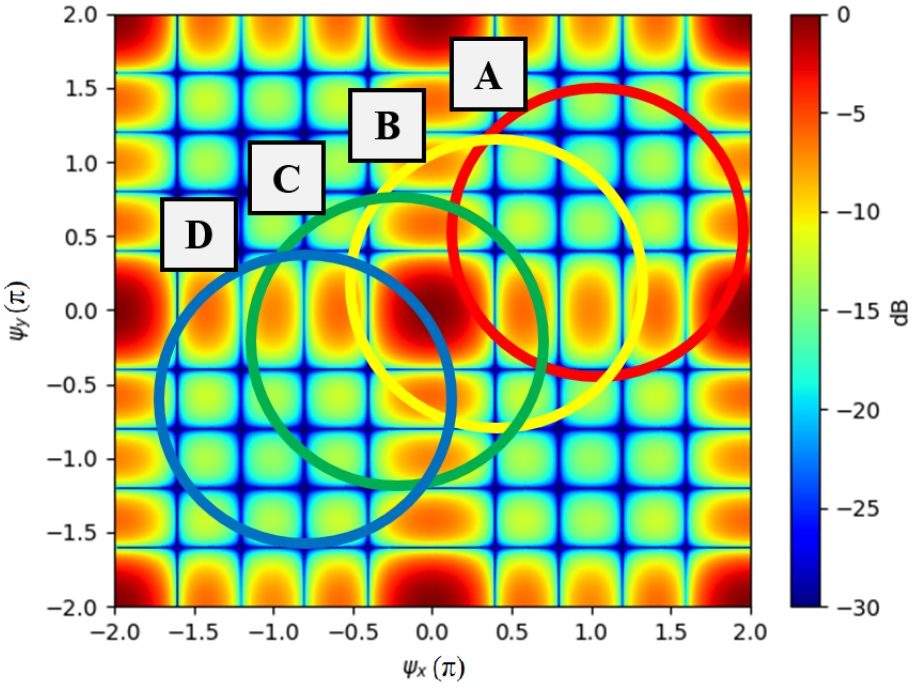

Figure 3.2. The normalised array factor $f(\psi_x, \psi_y)$ with visible regions indicated by various ellipses.

The array factor peak in the visible space regions B and C, corresponds to the physically possible reflected modes due to higher order diffraction values, $\eta_G = -1$ and $\eta_G = -2$, respectively. The direction $(\theta_r,\ \varphi_r)$ of these two reflected waves are calculated by simultaneously solving (3.2) and (3.3).

The predicted direction of the two reflected waves can also be calculated by determining the location of the peak of the array factor within the respective visible space. The peak of the visible space occurs when $\psi_x = 0$ and $\psi_y = 0$ [37]. By substituting $\psi_x = 0$, $\psi_y = 0$ and

($\theta = \theta_r$, $\varphi = \varphi_r$) into (3.10) and (3.11) the equations can be written as,

$$0 = \beta d_x(sin\theta_r cos\varphi_r - sin\theta_i cos(\varphi_i - \pi)) - \nabla\phi_x d_x(1 + \eta_G)$$

$$\beta sin\theta_r cos\varphi_r = \beta sin\theta_i cos(\varphi_i - \pi) + \nabla\phi_x(1 + \eta_G) \tag{3.15}$$

$$0 = \beta d_y(sin\theta_r sin\varphi_r - sin\theta_i sin(\varphi_i - \pi)) - \nabla\phi_y d_y(1 + \eta_G)$$

$$\beta sin\theta_r sin\varphi_r = \beta sin\theta_i sin(\varphi_i - \pi) + \nabla\phi_y(1 + \eta_G). \tag{3.16}$$

The reflected wave direction (θ_r, φ_r) can then be calculated by solving (3.15) and (3.16) simultaneously for different diffraction orders, η_G . These equations are almost exactly similar (only the σ element is not included) to the extended Snell's law equations (3.2) and (3.3) reinforcing the use of array theory to determine the scattering from a PGM as stated in, [3], [17] and [18].

As illustrated in Figure 3.2 the array factor displays peak values with a period of 2π in the x- and y-direction, respectively. This implies that the peak of the array factor is not necessarily $\psi_x = 0$, $\psi_y = 0$, but could be any of the peaks (grating lobes) observed in Figure 3.2. Equations (3.10) and (3.11) can thus be adjusted according to any of these peaks. This allows the calculation of the reflected wave when the visible space shifts over any of the array factor peaks.

The visible space regions A and D contain no peaks and correspond with non-valid diffraction order values which means (3.2) and (3.3) will return imaginary values for θ_r and no reflected waves are expected. Although there is no peak in ellipse D a significant portion of the ellipse intercepts with at least half of the peak at the centre of the normalised array factor and will result in reflected energy close to the plane of the PGM. The analogy to array theory [37] is that a significant portion (at least -3 dB) of the grating lobe appears in the visible space. A detailed method to determine if these regions overlap is given in Addendum A.

3.5 SIMULATION SETUP FOR SCATTERING FROM A PGM

An essential aspect of the metasurface design is the simulation environment used. The correct setup of the simulation environment ensures that the simulation results of the AMC elements and metasurfaces correlate with the final manufactured surface. The simulation environment consists of two different setups. The first is necessary to obtain reflection phase coefficients from various AMC elements used to design a PGM. The second setup is to obtain the bistatic and monostatic RCS of a metasurface.

3.5.1 AMC simulation environment

In [18] a single AMC element is designed by utilising a single cell with the appropriate boundary conditions. If the boundary conditions are correctly selected, the single AMC element will be equivalent to an infinite AMC structure of these elements [18]. The setup of this AMC simulation environment in CST is shown in Figure 3.3. The phase reflection vs. frequency curve of the AMC element is obtained using this method, and thus the AMC element can be optimised to the desired performance. An example of the phase reflection vs. frequency for varying AMC elements is shown in Figure 3.4.

In [51] a single band AMC element was designed with a resonating frequency at 2.45 GHz. The simulated results of this AMC element is obtained by using a waveguide feed in CST Studio Suite [21]. The boundary conditions suggested in [18] are used and noted in Table 3.1. The AMC element from [51] was simulated using CST Studio Suite [21] to compare the simulated phase reflection coefficient to the result given in [51]. The resonant reflection phase simulated at 2.44 GHz compared very closely to the specified resonant reflection phase of 2.45 GHz in [51] for the specified AMC element.

Table 3.1. Boundary conditions for AMC element (facing in the -z direction) simulation environment.

Boundary	Condition
X_{min}	Magnetic boundary ($H_t = 0$)
X_{max}	Magnetic boundary ($H_t = 0$)
Y_{min}	Electric boundary ($E_t = 0$)
Y_{max}	Electric boundary ($E_t = 0$)
Z_{min}	Open boundary
Z_{max}	Open boundary

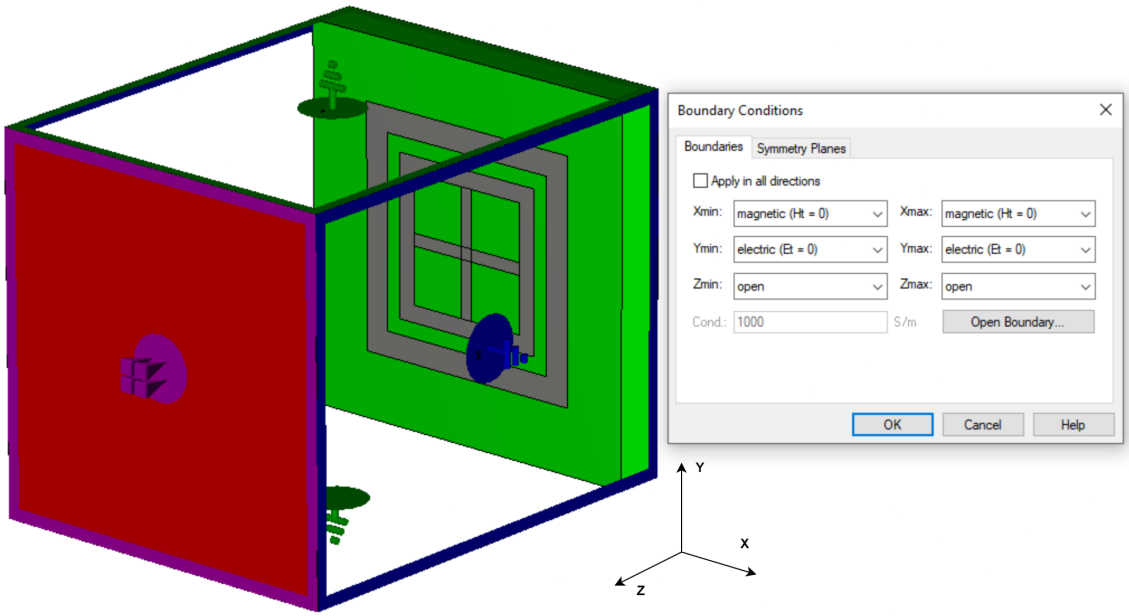

Figure 3.3. AMC simulation environment setup example from CST showing selected boundary conditions.

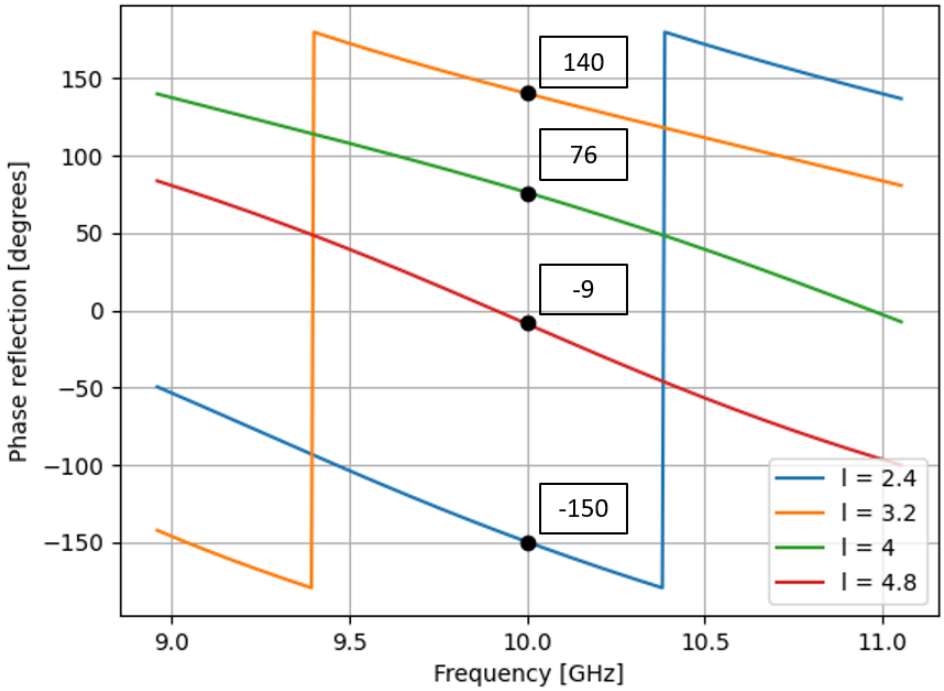

Figure 3.4. Phase reflection vs. frequency of AMC elements with varying parameters showing varying reflection phases.

3.5.2 Metasurface RCS simulation environment

The RCS simulation environment is easily verified. A simple object of which the RCS is known, such as a rectangular PEC plate or sphere, can be simulated and compared to the theoretically expected result. The theoretical RCS of a rectangular plate is calculated using,

$$\sigma_{max} = \frac{4\pi w^2 h^2}{\lambda^2}, \tag{3.17}$$

where h is the height of the plate, w the width of the plate and λ the wavelength of the incident wave. The theoretical RCS of a sphere of radius r is calculated with,

$$\sigma_{max} = \pi r^2. \tag{3.18}$$

Various solvers in CST Studio Suite could be used to simulate the RCS of a metasurface. The frequency-domain solver is based on the Finite Element Method (FEM) and is ideal for multi-port systems. The integral equation solver is based on the method of moments (MOM) technique and the multilevel fast multipole method (MLFMM) and uses surface integrals, making it more efficient than a full volume method when the model is large and contains lots of empty space. Lastly, the time domain solver is based on the finite integration technique (FIT) and transmission line matrix (TLM) and can perform broadband simulations in a single run. This solver also supports hardware acceleration, making it ideal for medium-large, complex, and detailed models. The size in wavelength of the PGMs that will be simulated are around 5 λ which put these models in the medium-large category. For these reasons the time domain solver was used for the simulated PGMs.

To validate the time domain solver settings a square PEC plate of 0.3 m $\times$ 0.3 m was simulated in CST and the result compared to the theoretical value equated with (3.17). The simulated RCS of the plate was approximately 14.4 dBm^2. The theoretical RCS of the plate was calculated as 14.5 dBm^2.

3.5.3 Design of a 3$\times$3 PGM for simulations

A PGM operating at 10 GHz was designed and used in simulations to investigate and validate the proposed method to predict the reflected wave directions

The phase gradient of the PGM is the phase variation between adjacent AMC elements on the PGM. A property of AMC elements is that the phase of the reflection coefficient varies with frequency while the magnitude of the reflection coefficient ideally stays close to unity. If this phase difference between adjacent AMC elements remains relatively stable over a wide frequency range, the phase gradient will be a constant value over this wide frequency band. This simple concept implies that AMC elements are capable of broadband RCS manipulation. The final design of the PGM is thus dependent on the selection and design of the AMC elements used to create the PGM.

The AMC elements used to design the PGMs analysed in this report were inspired by the design found in [10] and [40] and is shown in Figure 3.5. These AMC elements were implemented on Rogers 5880 substrate. The Rogers 5880 substrate has a relative dielectric constant of $\varepsilon_r = 2.2$ which is much lower than more commonly used substrate such as FR-4 which has an average relative dielectric constant of $\varepsilon_r = 4.3$ [52]. The lower dielectric constant allows a gradual phase reflection transition for a thinner substrate compared to a substrate with a higher dielectric constant. The parameters of the elements are defined in Figure 3.5. The optimum values for the AMC elements have been obtained exploiting the relevant CST tool and are summarised in Table 3.2.

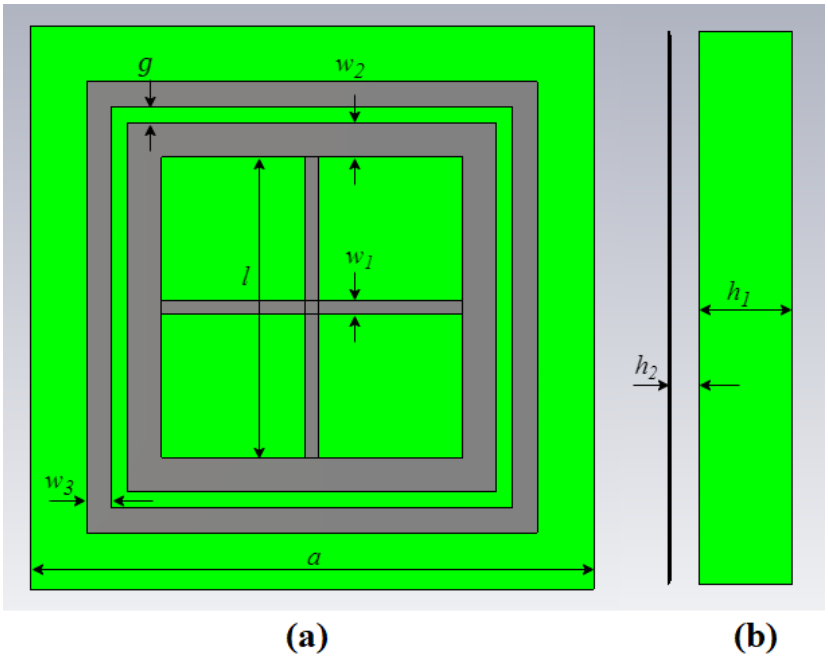

Figure 3.5. Geometry of the AMC element. (a) Top view. (b) Side view.

The parameter l determines the reflection phase coefficient of the AMC element. A phase variation of 2π rad between the subcells ensures the 4×4 AMC elements, forming a subcell, results in a periodic arrangement. The phase difference between the AMC elements was chosen as $\delta\phi_x = \frac{\pi}{2}$ rad and $\delta\phi_y = \frac{\pi}{2}$ rad at 10 GHz. The phase gradient, $\nabla\phi_{x,y}$, for this PGM, shown in Figure 3.6, can then be calculated as the change in phase, $\delta\phi_{x,y}$, over the width, a,

of the AMC element as,

$$\nabla\phi_{x,y} = \frac{\delta\phi_{x,y}}{a}. \tag{3.19}$$

Table 3.2. Parameters of the AMC elements operating at 10 GHz.

Symbol	Description	Value (mm)
a	width of AMC element	12.0
w_1	width of cross	0.4
w_2	width of inner square ring	1.1
w_3	width of outer square ring	0.8
g	gap between the rings	0.5
l	length of the cross (for 4 elements, respectively)	3.4, 4.2, 4.7, 5.6
h_1	height of the substrate	3.0
h_2	air gap between the substrate and the ground plane	1.0

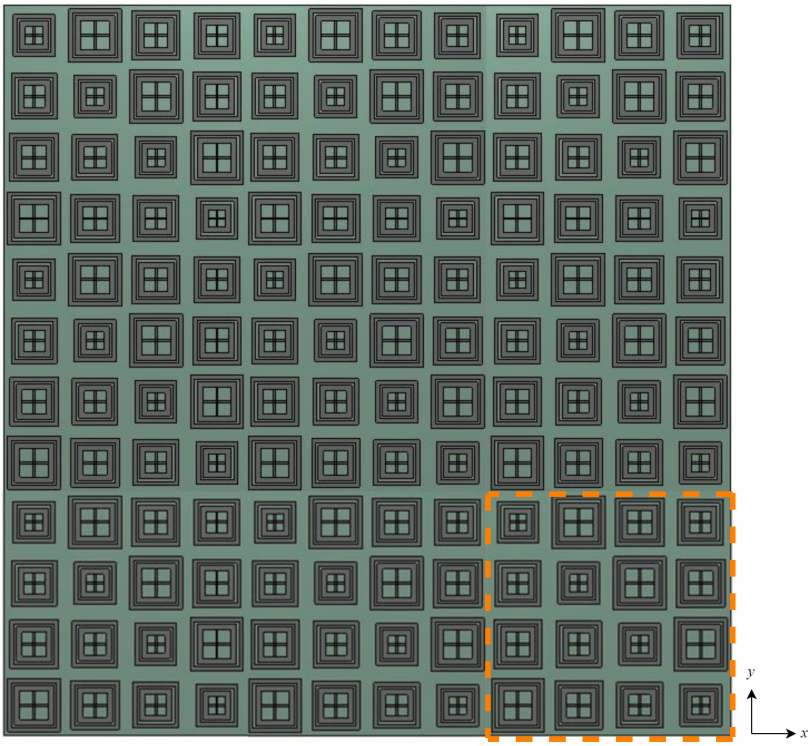

Figure 3.6. The front view of the resulting PGM using AMC elements described by Table 3.2. A subcell of 4×4 AMC elements is indicated by the dashed line.

3.6 SIMULATED RESULTS

In Sections 3.3 and 3.4 methods were proposed to determine the direction of the reflected waves of a PGM with dual phase gradients for an incident wave from an arbitrary direction. These methods are validated in this section by performing monostatic and bistatic RCS simulations in CST Studion Suite [21] for the PGMs described in Section 3.5.

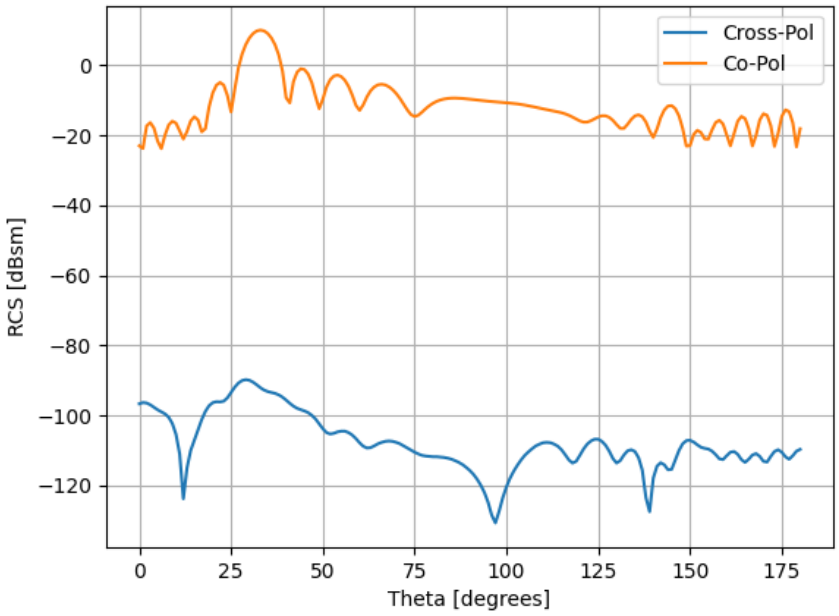

Figure 3.7. Co- and cross-polarisation magnitude comparison for an RCS simulation of the PGM.

Before conducting the detailed simulations on this PGM a comparison was done between the simulated co- and cross-polarisation magnitudes for a simulation as shown in Figure 3.7. This figure shows the cross-polarisation magnitude has negligible effect on the absolute RCS magnitude.

The bistatic RCS scattering result for an incident plane wave at $\theta_i = 60°$, $\varphi_i = 20°$ is shown in Figures 3.8 and 3.9. There are three distinct scattering directions at approximately ($\theta_1 = 60°$, $\varphi_1 = 200°$), ($\theta_2 = 25°$, $\varphi_2 = 115°$) and ($\theta_3 = 80°$, $\varphi_3 = 65°$).

The methods to predict these reflected waves as given in Sections 3.3 and 3.4 were compared to the simulated results. The values of the symbols required to predict the directions of the reflected waves for the incident plane wave from $\theta_i = 60°$, $\varphi_i = 20°$ are given in Table 3.3.

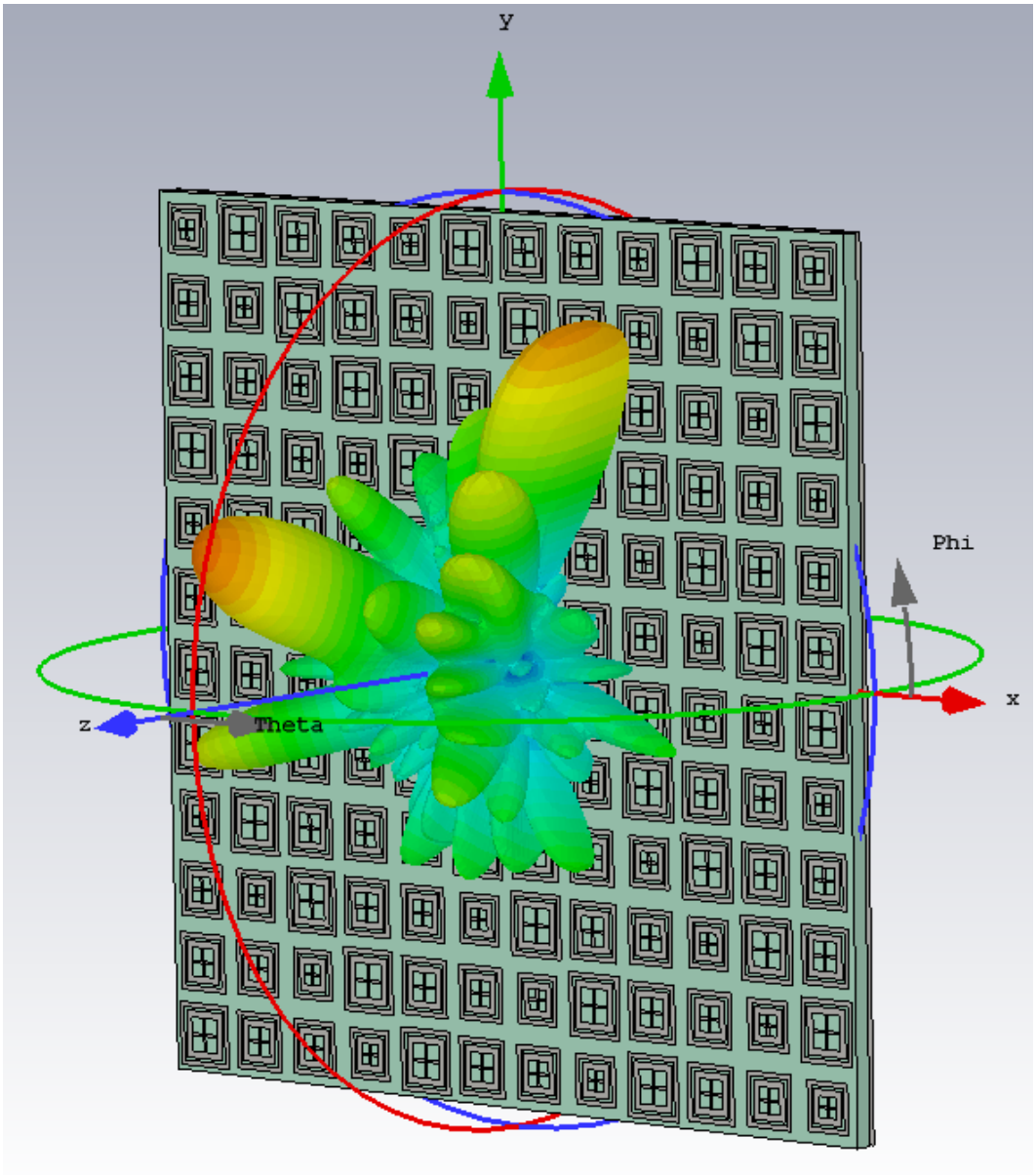

Figure 3.8. 3-D scattering pattern for an incident plane wave at $\theta_i = 60°$, $\varphi_i = 20°$

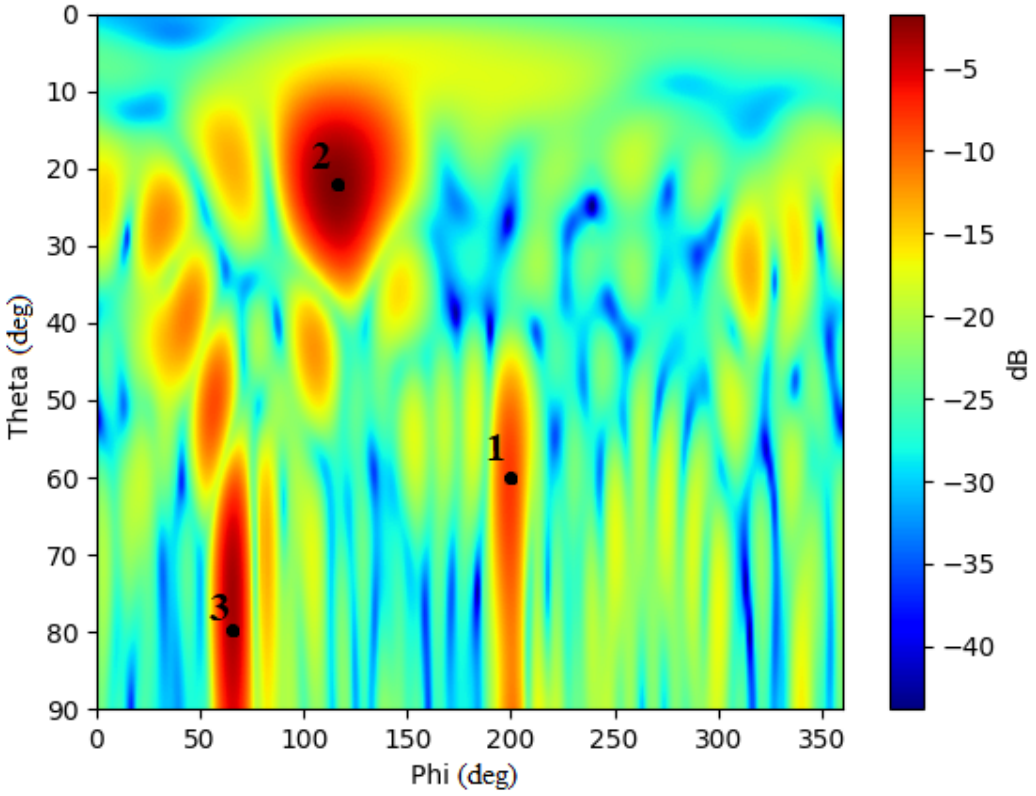

Figure 3.9. The bistatic scattering from the PGM, illustrating distinct reflection peaks.

Table 3.3. Values of symbols for reflection direction prediction for $\theta_i = 60°$, $\varphi_i = 20°$.

Symbol	Description	Value
θ_i	incident θ angle	60°
φ_i	incident φ angle	20°
β	phase constant $= \frac{2\pi}{\lambda}$	209.44 rad/m
λ	wavelength	30 mm
$d_{x,y}$	uniform spacing between adjacent elements on x- and y- axis, respectively	12 mm
$\nabla\phi_{x,y}$	phase gradients of the x- and y- axis, respectively. Expressed as the change in phase over distance.	-90°/12 mm
σ	direction of the phase gradient	-1

3.6.1 Predicting reflected wave directions using Snell's Law

In Section 3.3 the reformulated generalised Snell's law of reflection was extended to account for an incident wave from an arbitrary direction (θ_i, φ_i) and dual phase gradients ($\nabla\phi_x$, $\nabla\phi_y$) as shown in (3.2) and (3.3). The known values for these equations are given in Table 3.3. Various diffraction order values, (η_{Gx}, η_{Gy}), were substituted into (3.2) and (3.3) and then simultaneously solving these equations to calculate θ_r and φ_r. The direction of reflected waves calculated with various diffraction order modes are given in Table 3.4.

Table 3.4. Calculated results for various diffraction orders using expanded Snell's law method

η_G	θ_r	φ_r
1	1.57 - 1.91j rad	216.58°
0	1.57 - 1.13j rad	212.57°
-1	60°	200°
-2	22.28°	119.86°
-3	1.57 - 0.31j rad	65.32°

Two valid diffraction order modes produce real directions for reflected waves viz. $\eta_G = -1$ and $\eta_G = -2$ corresponding to the directions of the reflected waves at ($\theta_1 = 60°$, $\varphi_1 = 200°$) and ($\theta_2 = 22.28°$, $\varphi_2 = 119.86°$), respectively. These two calculated directions correspond very well with the simulated reflected waves labelled 1 and 2 shown in Figure 3.9.

3.6.2 Predicting reflected wave directions using antenna array theory

The φ_r direction of the diffraction order mode of $\eta_G = -3$ corresponds with the third simulated reflected wave (labelled 3), ($\theta_3 = 80°$, $\varphi_3 = 65°$), shown in Figure 3.9. However, for this diffraction order mode an imaginary θ_r angle was calculated. Section 3.4 was used to determine if this diffraction order mode caused the visible space to overlap with at least half of the peak at the centre of the normalised array factor as illustrated by ellipse D in Figure

3.2. This was done by calculating the visible space region for the current diffraction order, $\eta_G = -3$, then determining if at least -3 dB of the AF peak falls within this visible space region.

To determine if at least -3 dB of the AF peak falls within the visible space region the process from Addendum A was followed. Firstly the visible space region was calculated for the diffraction order $\eta_G = -3$. The centre of the region was calculated using (3.10) and (3.11) as,

$$\psi_x(\theta,\varphi) = \beta d_x(sin\theta cos\varphi - sin\theta_i cos(\varphi_i - \pi)) - \nabla\phi_x d_x(1+\eta_G)$$
$$\psi_x(0,0) = -0.35\pi \tag{3.20}$$
$$\psi_y(\theta,\varphi) = \beta d_y(sin\theta sin\varphi - sin\theta_i sin(\varphi_i - \pi)) - \nabla\phi_y d_y(1+\eta_G)$$
$$\psi_y(0,0) = -0.67\pi. \tag{3.21}$$

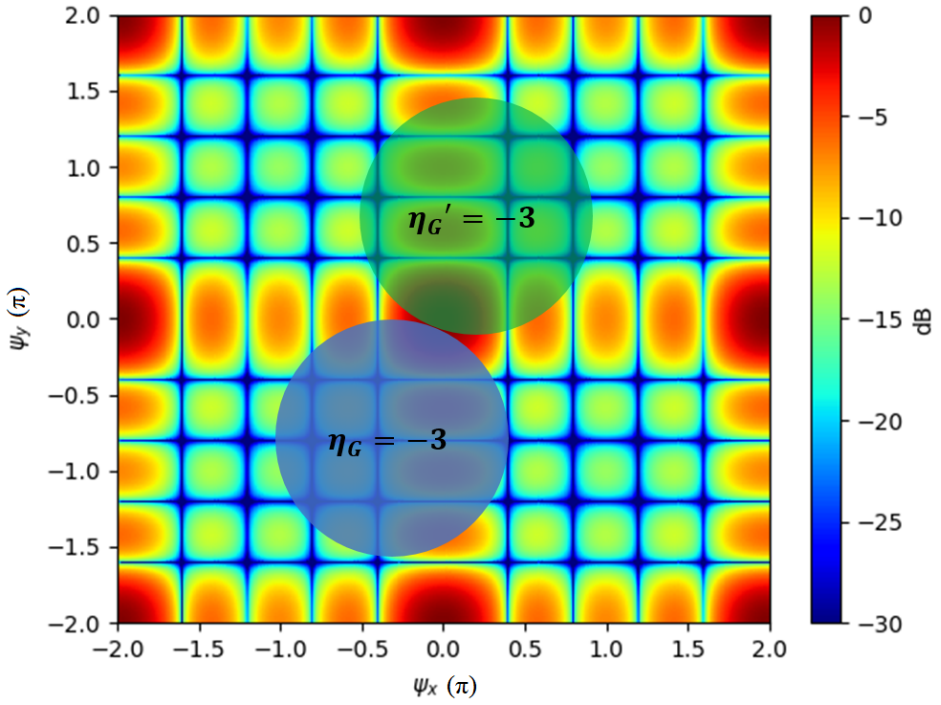

Figure 3.10. Visible space region for diffraction order, $\eta_G = -3$, and shifted visible space region, η_G', indicated on array factor plot.

The visible space region shown in Figure 3.10 was calculated using (3.12) and (3.13) as,

$$\psi_x(0,0) - \beta d_x < \psi_x < \psi_x(0,0) + \beta d_x$$

$$-1.15\pi < \psi_x < 0.45\pi \tag{3.22}$$

$$\psi_y(0,0) - \beta d_y < \psi_y < \psi_y(0,0) + \beta d_y$$

$$-1.56\pi < \psi_y < 0.04\pi. \tag{3.23}$$

The visible space region was then shifted towards the array factor peak by two times the radius of the ellipse which describes the visible space. Equations (A.1) to (A.7) were used to calculate the region of the shifted visible space as illustrated in Figure A.2. First x_e and y_e was calculated as,

$$\theta = \arctan\left(\frac{\psi_x(0,0)}{\psi_y(0,0)}\right) = 65.46^\circ \tag{3.24}$$

$$x_e = \beta d_x cos\theta = 209.44 \times 0.012 \times \cos 65.46^\circ = 0.33\pi \tag{3.25}$$

$$y_e = \beta d_y sin\theta = 209.44 \times 0.012 \times \sin 65.46^\circ = 0.73\pi. \tag{3.26}$$

The centre of the visible space was then calculated using (A.3) and (A.4) as,

$$x' = \psi_x(0,0) + 2x_e = 0.31\pi \tag{3.27}$$

$$y' = \psi_y(0,0) + 2y_e = 0.69\pi. \tag{3.28}$$

Lastly the direction of the reflected wave for the shifted visible space is calculated by substituting the calculated values from (3.25)-(3.28) into (A.3) and (A.4) and simultaneously solving for θ_r and φ_r as,

$$\theta_{r_{shift}} = 72.30^\circ \tag{3.29}$$

$$\varphi_{r_{shift}} = 245.74^\circ. \tag{3.30}$$

The half power beamwidth (HPBW) for the reflected wave was calculated with (A.10) as,

$$HPBW = \frac{2 \times 2\pi}{N} = 144^{\circ}. \tag{3.31}$$

The criteria in A.11 was used to determine if this diffraction order mode is valid as,

$$\theta_{r_{shift}} + \frac{HPBW}{2} = 149.3^{\circ} > 90^{\circ}. \tag{3.32}$$

The reflected wave -3 dB region is not fully contained within the shifted visible space and thus overlaps with the original visible space region which indicates at least -3 dB of the array factor peak falls within the visible space region for the diffraction order, $\eta_G = -3$. This indicates that the reflected wave produced by this diffraction order mode will have significant power (at least -3 dB) at the plane of the PGM at the calculated $\varphi_r = 65.32^{\circ}$. This prediction correlates very closely with the simulated result in Figure 3.9.

In summary using the expanded Snell's law to predict the reflected wave directions as well as the array theory approach approximation three distinct reflected waves were predicted. These predictions are compared to the simulated results in Table 3.5 and show great correlation with each other.

Table 3.5. Summary of predicted vs. simulated reflected wave directions.

η_G	**Predicted** θ_r	**Predicted** φ_r	**Simulated** θ_r	**Simulated** φ_r
-1	60°	200°	60°	200°
-2	22.28°	119.86°	25°	115°
-3	90°	65.42°	80°	65°

3.6.3 Additional simulations

Additional simulations with varying incident angles were conducted for the dual-phase gradient metasurface from Section 3.5.3. The observed wave directions, predicted wave directions and valid diffraction orders are summarised in Table 3.6. The simulated results and additional relevant information for these simulations are given in Addendum B.

Table 3.6. Additional simulated and predicted results for various incident angles.

Incident Angle		**Simulated Peak Directions**		**Predicted Peak Directions**		**Valid Diff. Orders**	**Notes**
θ_i	φ_i	θ_r	φ_r	θ_r	φ_r	η_G	
30.6°	22.4°	26°	70°	27.1°	70.3°	-2	
		30°	200°	30.6°	202.4°	-1	
40°	45°	85°	45°	90°	45°	-3	HPBW method
		14°	45°	13.95°	45°	-2	
		40°	225°	40°	225°	-1	
70°	135°	55°	135°	55.9°	135°	-3	AF peak at
		70°	315°	70°	315°	-1	$\psi_x = -2\pi$, $\psi_y = 0$
30°	160°	30°	340°	30°	340°	-1	
		55°	260°	54.19°	258.97°	0	
60°	200°	60°	20°	60°	20°	-1	
		20°	300°	22.28°	299.97°	0	
60°	340°	80°	290°	90°	294.57°	-3	HPBW method with
		59°	100°	70.1°	101.6°	-2	AF peak at
		60°	160°	60°	160°	-1	$\psi_x = 0$, $\psi_y = -2\pi$

The compared results given in Table 3.6 show that the predicted results using the method presented in this study compare very well with the simulated result for a dual-phase gradient metasurface for different incident angles. The incident angles given in Table 3.6 include angles from each quadrant which exceed the critical incident value as well as angles that

do not exceed this critical incident value. The *Notes* column of the table describes when the reflected wave direction was not determined by simply simultaneously solving (3.2) and (3.3). When the array factor method given in Addendum A was used to determine if the selected diffraction order was valid the note given is "HPBW method". If the visible space shifts over an AF peak other than the peak at ($\psi_x = 0$, $\psi_y = 0$) then (3.10) and (3.11) can be simultaneously solved with the correct AF peak substituted in to solve for the predicted reflected wave direction.

3.6.4 Investigation of multiple valid diffraction order modes

The introduction of the diffraction order into the generalised Snell's law of reflection presented in [15] provided a solution to the critical value issue which caused the reflected wave direction to be calculated as an imaginary value. The addition of the diffraction order mode is however only used for incident angles that exceed the critical value. From the various simulations done it was seen that multiple diffraction orders are valid for a single incident angle. Most cases simulated were however scenarios where the incident angle exceeded the critical value. Multiple valid diffraction orders are also expected for angles less than the critical value, as the periodicity of the phase gradient will still have an influence on the reflected wave direction.

To confirm this hypothesis a bistatic simulation was performed for an incident angle of $\theta_i = 0^\circ$ on a 2×6 PGM (design parameters given in Table 3.2) with a phase gradient in only one direction, the x-axis ($\nabla\phi_x = \frac{-90^\circ}{12\,\text{mm}}$, $\nabla\phi_y = 0$). The incident angle, θ_i, φ_i, was varied only in the θ direction, with constant $\varphi_i = 0^\circ$. By substituting various diffraction orders into (3.2) and (3.3) and simultaneously solving these equations it was seen that there were multiple valid diffraction orders that provide real reflected wave directions. The reflected waves are predicted at $\theta_{r1} = -38.68^\circ$ for the diffraction order $\eta_G = 0$, $\theta_{r2} = 0^\circ$ for $\eta_G = -1$ and $\theta_{r3} = 38.68^\circ$ for $\eta_G = -2$.

A 2×6 PGM adds more periodicity to the axis that contains the phase gradient. The scattering

from this metasurface can be seen in Figures 3.11 and 3.12. Three distinct reflected waves are seen at $\theta_{r1} = -39^\circ$, $\theta_{r2} = 0^\circ$ and $\theta_{r3} = 38^\circ$ which correspond very well with the three predicted waves.

This simulation also confirms the hypothesis that there can be multiple valid diffraction orders for any incident angle, less than the critical angle and exceeding the critical angle. The method of reflected wave direction prediction provided by this study is thus confirmed to be valid for arbitrary incident angles.

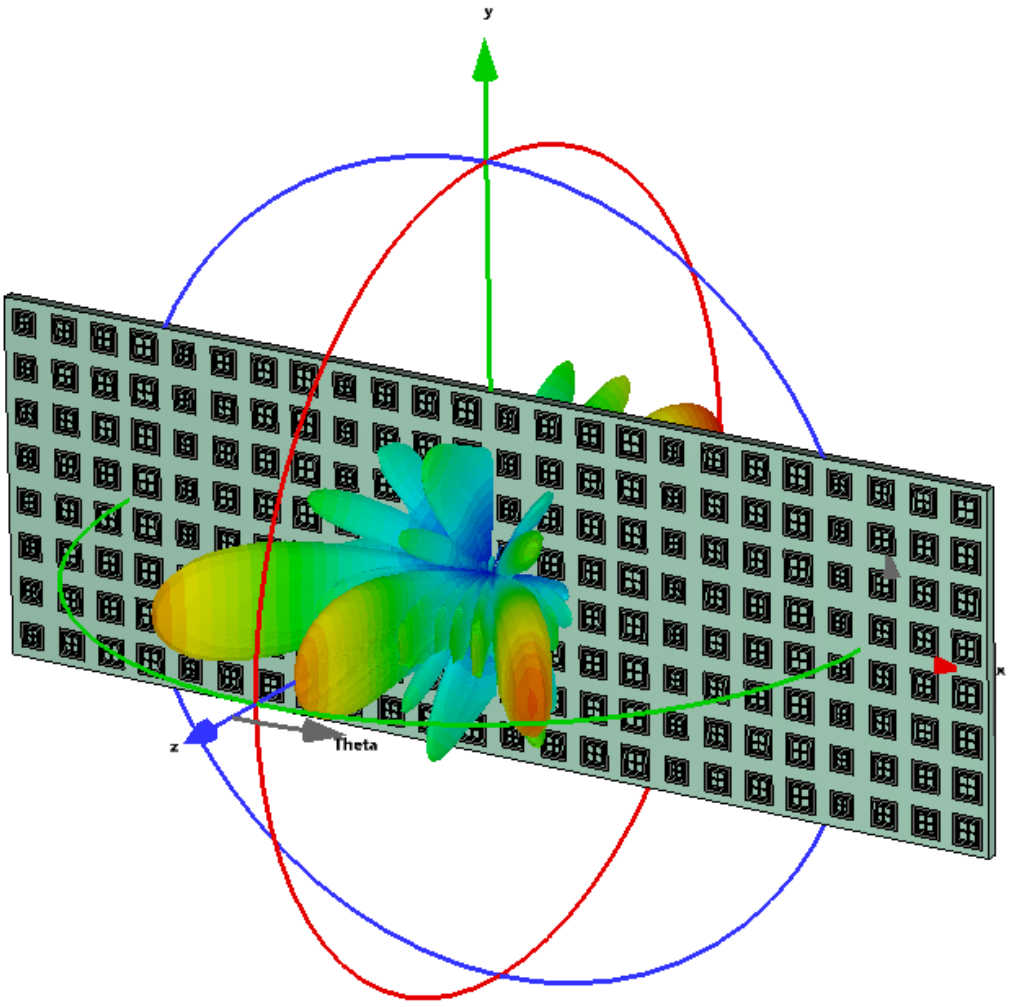

Figure 3.11. 3-D scattering pattern for incident plane wave at $\theta_i = 0^\circ$, $\varphi_i = 0^\circ$ for 2×6 PGM.

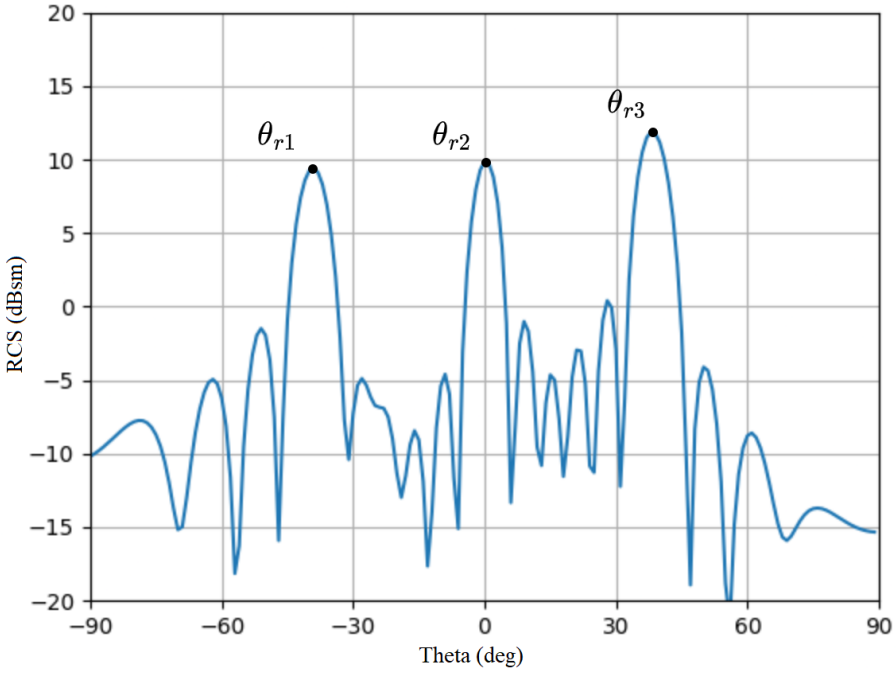

Figure 3.12. Bistatic simulation result for an incident angle of $\theta_i = 0°$ for 2×6 PGM. Three peaks are observed at $\theta_{r1} = -39°$, $\theta_{r2} = 0°$ and $\theta_{r3} = 38°$.

3.7 SUMMARY

In this chapter, a method was developed to calculate various reflected wave directions for a PGM with dual-phase gradients with an incident plane wave from an arbitrary angle. Snell's law was reformulated in [15] and [19] to include a diffraction order element. The reformulated Snell's law was extended to account for an incident wave from an arbitrary direction (θ_i, φ_i) with dual-phase gradients in the x- and y-direction. A method to determine the direction of the additional energy [16] close to the plane of the PGM was also developed. It was shown that a PGM can be analysed as an equally spaced uniformly excited array. The normalised array factor for an equally spaced uniformly excited array was adapted to the scattering from a PGM with a dual-phase gradient. It was shown that the additional energy close to the plane of the PGM occurred when there is significant overlap between the grating lobe and the visible space.

The simulation environment setup used to validate the prediction method was discussed. The AMC simulation environment setup was shown with the necessary boundary conditions to obtain accurate results. The RCS simulation environment was also discussed and verified by comparison of the theoretical RCS of a PEC plate with the simulated RCS of the same plate. The design of a PGM, operating at 10 GHz, for simulations was also illustrated. The PGM consisted of 3×3 subcells, where each subcell was made up by 4×4 AMC elements. This PGM was used in simulations to investigate and validate the proposed method to predict the reflected wave directions. The PGM consists of a dual-phase gradient.

The simulated results were then presented which were used to successfully validate the proposed method of prediction. CST Studio Suite [21] was used to simulate numerous scenarios for various incident angles with the designed PGM. The scattered reflected wave directions were predicted using the proposed method in this chapter and showed great correlation with the observed reflected wave directions. Comparison of simulations and predictions for various incident angles from all quadrants showed great comparison.

Lastly an investigation was done to verify whether the proposed method of prediction is valid for arbitrary incident angles and not only angles exceeding the critical value. A PGM with a single phase gradient was selected for the investigation. For such a PGM multiple diffraction orders were predicted to be valid with an incident angle not exceeding the critical value. A PGM with a 2×6 subcell layout, also with 4×4 AMC elements per subcell but only a single-phase gradient, was simulated. The observed reflected wave directions compared very well with the predicted directions.

CHAPTER 4 MEASURED RESULTS

4.1 CHAPTER OVERVIEW

Various measured RCS results are presented in this chapter. These results are used to verify the simulated results and the proposed method to predict the reflected wave directions presented in Chapter 3. The design of a prototype PGM is discussed in Section 4.2. The AMC elements used for this PGM were optimised to operate at 5 GHz using the AMC element from Section 3.5.3 as a design starting point.

Monostatic RCS measurements were conducted in the CATR at the University of Pretoria to verify the simulated results as well as the proposed method to predict the reflected wave directions. The monostatic RCS measurement setup, measured results as well as comparison of predicted reflected wave directions are given in Section 4.3.

Bistatic RCS measurements were also performed. Traditionally the CATR is used for antenna characterisation and monostatic RCS measurements, but was reconfigured to perform bistatic RCS measurements. This reconfigured setup, measured results and comparison of the predicted reflected wave directions are discussed in Section 4.4.

4.2 DESIGN OF A 3×3 PROTOTYPE PGM FOR MEASUREMENTS

A PGM designed to operate at 5 GHz was manufactured and measured in the compact antenna range. The PGM consisted of an FR-4 substrate with no air gap between the substrate and the ground plane. The design of the AMC elements for this PGM used the AMC element from Section 3.5.3 as the starting point. A few design limitations were imposed on the prototype. The first limitation was to design only a single phase gradient for the PGM. This was done as the measurements would be conducted in only one cut plane of the PGM ensuring the anomalous reflected waves would fall in this measured cut plane. The AMC elements were adjusted and optimised using CST Studio Suite [21] for a phase difference of $\delta\phi_x = \frac{-\pi}{2}$ rad and $\delta\phi_y = 0$ rad. The second limitation was to ensure that the distance between the target and the receiver is larger than the far-field distance. The minimum separation between the PGM and the receiver antenna in the CATR was selected as 3 m, specifically for the bistatic measurements as a beam of this length would need to be connected to the azimuth pedestal of the CATR. This limitation resulted in a PGM (0.288 m × 0.288 m) which consisted of a maximum of 12×12 AMC elements to ensure the far-field distance between the target and receiver was less than 3 m. The prototype PGM can be seen in Figure 4.1 with the parameters of the AMC elements given in Table 4.1.

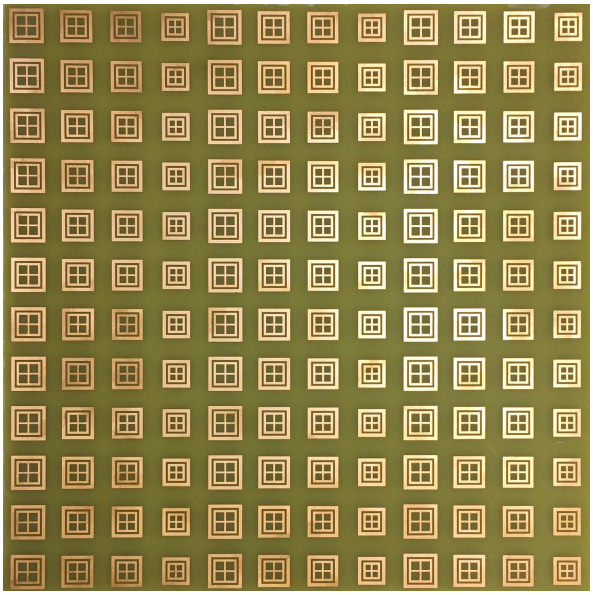

Figure 4.1. AMC element layout for the PGM measured in the compact range.

Table 4.1. Parameters of the AMC elements for the prototype PGM operating at 5 GHz.

Symbol	Description	Value (mm)
a	width of AMC element	24.0
w_1	width of cross	0.8
w_2	width of inner square ring	1.1
w_3	width of outer square ring	1.6
g	gap between the rings	1.0
l	length of the cross (for 4 elements, respectively)	6.0, 7.6, 8.1, 9.2
h_1	height of the substrate	6.4
h_2	air gap between the substrate and the ground plane	0.0

4.3 MONOSTATIC RCS MEASUREMENTS

A monostatic RCS measurement was conducted for the prototype PGM in the CATR at the University of Pretoria, South Africa. Traditionally the CATR is used for antenna characterisation and monostatic RCS measurements. The objective of the monostatic RCS measurement is to compare the result of the measurements with simulated results and finally verify the proposed method of reflected wave direction prediction posed in this study. A limitation of conducting a monostatic RCS measurement is that the incident wave direction (θ_i) and reflected wave direction (θ_r) will always be equal to each other. This implies that it will not be possible to measure multiple reflected modes at once. Only the reflected wave directions which are equal to the incident wave directions will be observed and these instances can be used to verify that the proposed method predicted the direction and mode of the observed reflected wave direction.

4.3.1 Monostatic RCS measurement setup

The monostatic RCS measurement setup in the CATR is shown in Figure 4.2. The PGM is illuminated with a plane wave from the reflector and the scattered field measured with the

same antenna used to illuminate the reflector. The PGM was rotated in azimuth, θ. This rotation angle (θ) is equal to the direction of the incident wave (θ_i) and the reflected wave direction (θ_r). The monostatic measurement setup, with the PGM mounted on a polystyrene column, in the compact range is shown in Figure 4.3. The coupling between the receiver and incident plane wave was eliminated using time gating during the measurements. The calibration was performed with a conducting sphere with a diameter of 153 mm.

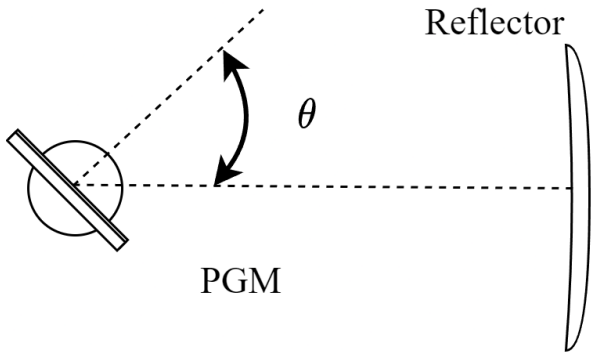

Figure 4.2. Monostatic measurement setup of the PGM. The PGM is illuminated with a plane wave from the reflector and the scattered field measured with the same antenna used to illuminate the reflector. The PGM was rotated in azimuth, θ.

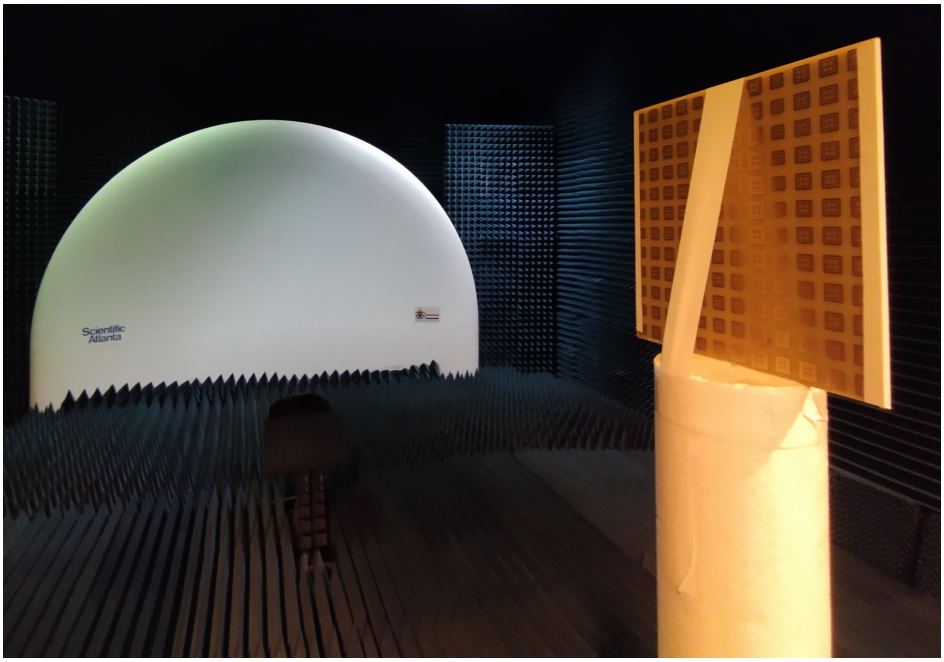

Figure 4.3. Monostatic measurement setup of the compact range.

4.3.2 Monostatic measurement results

A monostatic measurement was performed on the manufactured PGM detailed in Section 4.2. A simulation was also done in CST Studio Suite [21] for comparison. The simulated and measured results are shown in Figure 4.4. Three distinct reflected peaks are observed at $\theta_{r_1} = 18°$, $\theta_{r_2} = -38°$ and $\theta_{r_3} = -69°$. These peaks represent the direction of the reflected waves. As this is a monostatic RCS measurement the incident wave direction (θ_i) will be equal to the reflected wave direction (θ_r). The method to predict the direction of the reflected waves proposed by this study was then used to predict the reflected wave directions for the incident wave directions given by the observed peak.

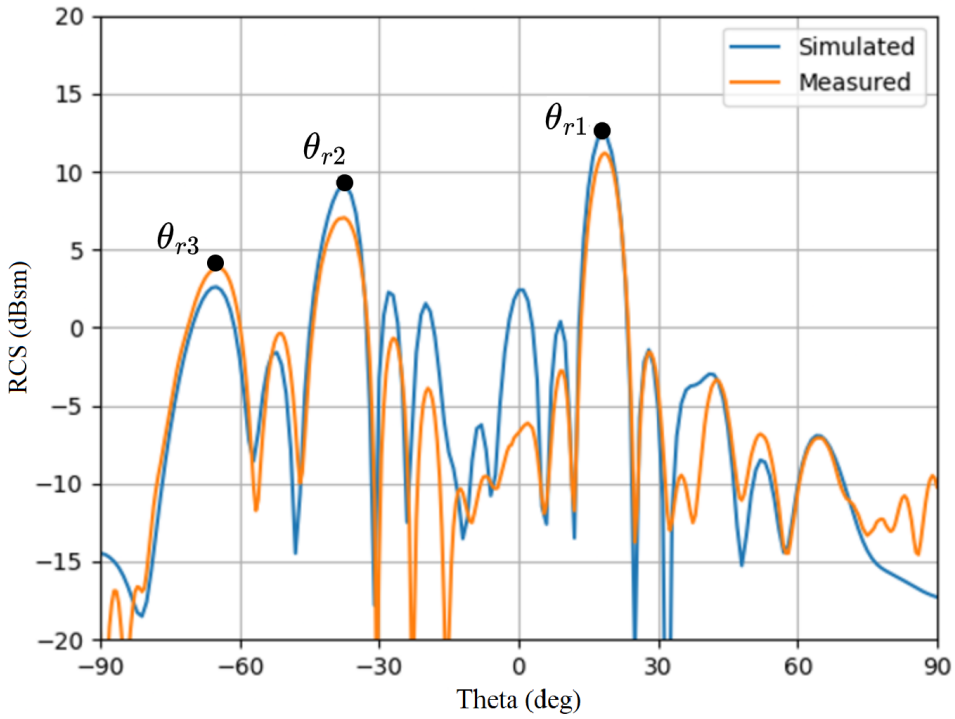

Figure 4.4. Monostatic measurement (VV polarisation) and simulation result.

Table 4.2. Values of symbols for reflection direction prediction.

Symbol	Description	Value
β_{5GHz}	phase constant $= \frac{2\pi}{\lambda}$	104.72 rad/m
λ_{5GHz}	wavelength	60 mm
$d_{x,y}$	uniform spacing between adjacent elements on x- and y- axis, respectively	24 mm
$\nabla\phi_x$	phase gradients of the x-axis. Expressed as the change in phase over distance.	-90°/24 mm
$\nabla\phi_y$	phase gradients of the y- axis. Expressed as the change in phase over distance.	0
σ	direction of the phase gradient	-1

The values of the symbols required to predict the directions of the reflected wave are given in Table 4.2. The first reflected peak was observed at $\theta_{r_1} = 18°$. The predicted reflected wave directions were then calculated using the incident angle of $\theta_i = 18°$. The active diffraction order modes and corresponding reflected wave directions for this incident angle is summarised in Table 4.3. With an incident wave direction of $\theta_i = 18°$ four active diffraction order modes are predicted as $\eta_G = [-3,-2,-1,0]$. This implies that if a bistatic RCS measurement was conducted for an incident wave direction of $\theta_i = 18°$ four reflected wave directions (θ_r) would be expected at the calculated directions given in Table 4.3. As this is a monostatic measurement only a reflected wave direction which is equal to the incident wave direction can be observed. From Table 4.3 the diffraction order of $\eta_G = -2$ results in a predicted reflected wave direction of $\theta_r = 18.42°$. This predicted reflected wave direction corresponds very closely with the observed measured and simulated peak in Figure 4.4.

Table 4.3. Predicted reflected waves for monostatic measurement with $\theta_i = 18°$.

η_G	θ_r	φ_r
-3	70.22°	0°
-2	18.42°	0°
-1	18°	180°
0	69.1°	180°

The second reflected peak was observed at $\theta_{r_2} = -38°$. With an incident angle of $\theta_i = -38°$ the reflected wave directions were calculated. The active diffraction order modes and corresponding reflected wave directions for this incident angle is summarised in Table 4.4. For this incident wave direction three active diffraction order modes are predicted as $\eta_G = [-1,0,1]$. Again this implies that three distinct reflected wave directions are expected with a bistatic RCS measurement for this incident angle. Due to the nature of a monostatic RCS measurement only the reflected wave directions which are equal to the incident wave directions can be observed. From Table 4.4 the diffraction order of $\eta_G = 1$ results in a predicted reflected wave direction of $\theta_r = -39.37°$. This predicted reflected wave direction corresponds very closely with the observed measured and simulated peak.

Table 4.4. Predicted reflected waves for monostatic measurement with $\theta_i = -38°$.

η_{Gx}	θ_r	φ_r
-1	38°	0°
0	0.54°	180°
1	39.37°	180°

The third reflected peak was observed at $\theta_{r_2} = -69°$. With an incident angle of $\theta_i = -69°$ the reflected wave directions were calculated. The active diffraction order modes and corresponding reflected wave directions for this incident angle is summarised in Table 4.5. Four active diffraction order modes are predicted as $\eta_G = [-1,0,1,2]$. From Table 4.5 the diffraction

order of $\eta_G = 2$ results in a predicted reflected wave direction of $\theta_r = -70.29°$. This predicted reflected wave direction corresponds very closely with the observed measured and simulated peak.

Table 4.5. Predicted reflected waves for monostatic measurement with $\theta_i = -69°$.

η_{Gx}	θ_r	φ_r
-1	69°	0°
0	17.97°	0°
1	18.45°	180°
2	70.29°	180°

Concluding the monostatic measurements the three distinct observed peaks in the monostatic RCS measurements were all successfully predicted by the method proposed in this study. Each peak corresponded to an active diffraction order mode and included incident angles below, (θ_{r_1}), and above, (θ_{r_2}, θ_{r_3}), the critical value of incidence discussed earlier in the study.

4.3.3 Additional monostatic measurement results

The AMC elements designed for the manufactured PGM have a phase gradient of $90°/24$ mm at 5 GHz. These AMC elements show a relatively stable phase reflection difference over a wide frequency band (± 20 % fractional bandwidth). The proposed method can thus be tested on other frequencies within the operational bandwidth of the AMC elements.

Monostatic measurements were performed on the manufactured PGM detailed in Section 4.2 at 4.5 GHz and 5.5 GHz which is at the edge of the 20 % fractional bandwidth of the centre frequency of 5 GHz.

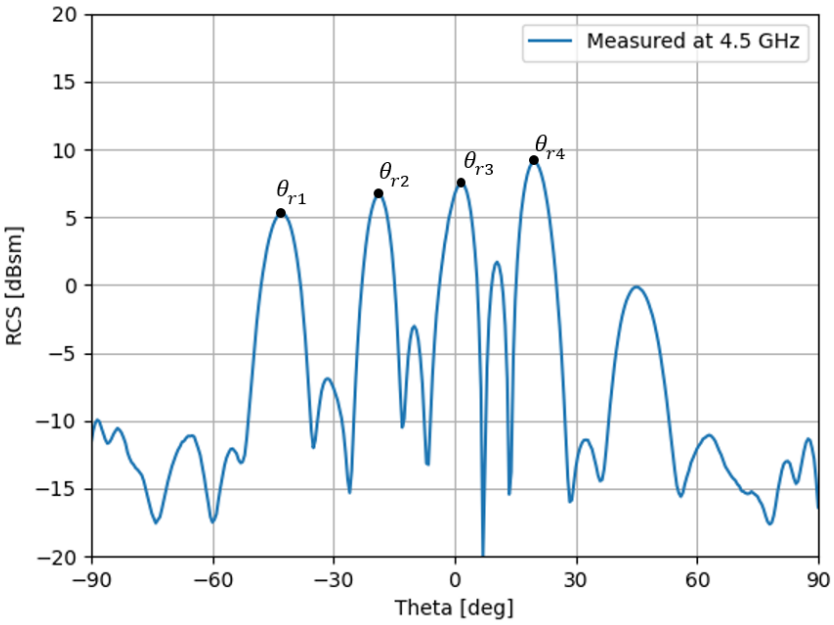

Figure 4.5. Monostatic measurement (VV polarisation) at 4.5 GHz.

The monostatic measured result at 4.5 GHz is shown in Figure 4.5. Four distinct peaks are observed at $\theta_{r_1} = -43°$, $\theta_{r_2} = -19°$, $\theta_{r_3} = 1°$ and $\theta_{r_4} = 19°$. The same method of comparison is used as discussed in Section 4.3.2. The values of the symbols required to predict the directions of the reflected waves are given in Table 4.2 with the exception of $\lambda = 67$ mm leading to $\beta_{4.5GHz} = 94.25$ rad/m due to the frequency change.

The first peak was observed at $\theta_{r_1} = -43°$. For an incident wave of $\theta_i = -43°$ three valid diffraction order modes are predicted as $\eta_G = [-1, 0, 1]$. The diffraction order mode of $\eta_G = 1$ results in a predicted reflected wave direction of $\theta_r = -44.98°$. This predicted reflected wave direction corresponds very closely with the observed measured peak θ_{r_1}. The slight discrepancy can be attributed to the fact that a perfect phase reflection difference of 90° is being used when the true phase reflection difference between the AMC elements will start to deviate as the operating frequency moves further from the designed centre frequency.

The second peak was observed at $\theta_{r_2} = -19°$. For an incident wave of $\theta_i = -19°$ two valid

diffraction order modes are predicted as $\eta_G = [-1, 0]$. The diffraction order mode of $\eta_G = 0$ results in a predicted reflected wave direction of $\theta_r = -21.65°$. This predicted reflected wave direction corresponds very closely with the observed measured peak θ_{r_2}.

The third peak was observed at $\theta_{r_3} = 1°$. For an incident wave of $\theta_i = 1°$ three valid diffraction order modes are predicted as $\eta_G = [-2, -1, 0]$. The diffraction order mode of $\eta_G = -1$ results in a predicted reflected wave direction of $\theta_r = -0.97°$. This predicted reflected wave direction corresponds very closely with the observed measured peak θ_{r_3}.

The fourth peak was observed at $\theta_{r_4} = 19°$. For an incident wave of $\theta_i = 19°$ two valid diffraction order modes are predicted as $\eta_G = [-2, -1]$. The diffraction order mode of $\eta_G = -2$ results in a predicted reflected wave direction of $\theta_r = 21.67°$. This predicted reflected wave direction corresponds very closely with the observed measured peak θ_{r_4}.

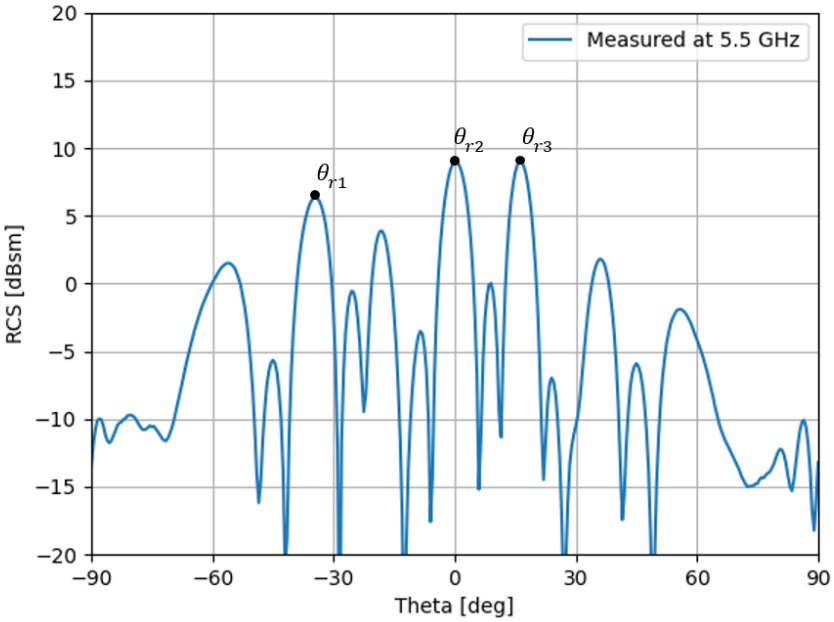

Figure 4.6. Monostatic measurement (VV polarisation) at 5.5 GHz.

The monostatic measured result at 5.5 GHz is shown in Figure 4.6. Three distinct peaks are observed at $\theta_{r_1} = -35°$, $\theta_{r_2} = 0°$ and $\theta_{r_3} = 16°$. The same method of comparison is used

as discussed in Section 4.3.2. The values of the symbols required to predict the directions of the reflected waves are given in Table 4.2 with the exception of $\lambda = 55$ mm leading to $\beta_{5.5GHz} = 115.19$ rad/m due to the frequency change.

The first peak was observed at $\theta_{r_1} = -35^\circ$. For an incident wave of $\theta_i = -35^\circ$ three valid diffraction order modes are predicted as $\eta_G = [-1, 0, 1]$. The diffraction order mode of $\eta_G = 1$ results in a predicted reflected wave direction of $\theta_r = -34.25^\circ$. This predicted reflected wave direction corresponds very closely with the observed measured peak θ_{r_1}.

The second peak was observed at $\theta_{r_2} = 0^\circ$. For an incident wave of $\theta_i = 0^\circ$ three valid diffraction order modes are predicted as $\eta_G = [-2, -1, 0]$. The diffraction order mode of $\eta_G = -1$ results in a predicted reflected wave direction of $\theta_r = 0^\circ$. This predicted reflected wave direction is exactly the same as the observed measured peak θ_{r_2}.

The third peak was observed at $\theta_{r_3} = 16^\circ$. For an incident wave of $\theta_i = 16^\circ$ four valid diffraction order modes are predicted as $\eta_G = [-3, -2, -1, 0]$. The diffraction order mode of $\eta_G = -2$ results in a predicted reflected wave direction of $\theta_r = 17.01^\circ$. This predicted reflected wave direction corresponds very closely with the observed measured peak θ_{r_3}.

4.4 BISTATIC RCS MEASUREMENTS

The manufactured PGM discussed in Section 4.2 was also measured in the CATR at the University of Pretoria with a bistatic RCS measurement setup. The objective of the bistatic RCS measurement is to again compare the measured results with simulated bistatic results and finally verifying the proposed method of reflected wave direction prediction. The advantage of the bistatic RCS measurement is that various reflected wave directions (θ_r) can be measured for a single incident angle (θ_i) which was not possible for the monostatic RCS measurements.

4.4.1 Bistatic RCS measurement setup

Traditionally the compact range is used for antenna characterisation and monostatic RCS measurements. It was reconfigured to perform bistatic RCS measurements, as shown in Figure 4.7. The PGM is illuminated with a plane wave from the reflector and the scattered field measured with a wideband receive antenna at a fixed distance and bistatic angle γ relative to the PGM. The PGM and receive antenna were rotated in azimuth, θ.

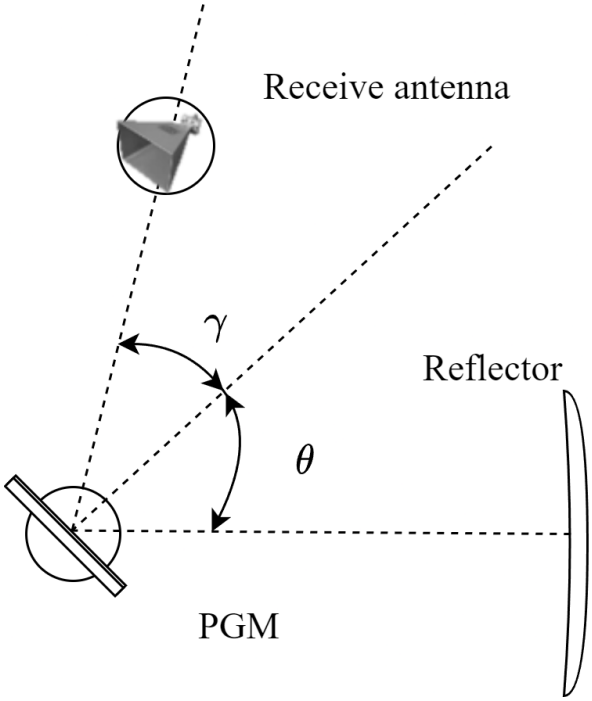

Figure 4.7. Bistatic measurement setup of the PGM. The PGM is illuminated with a plane wave from the reflector and the scattered field measured with a wideband receive antenna at a fixed distance and bistatic angle γ relative to the PGM. The PGM and receive antenna were rotated in azimuth, θ.

The bistatic RCS measurements were conducted by mounting the PGM on the azimuth pedestal of the compact range using a polystyrene column, illuminating the PGM with a plane wave created by an offset parabolic reflector and measuring the scattered field with a wideband receive antenna at a fixed bistatic angle, γ, relative to the PGM as shown in Figure 4.8. The receive antenna was also mounted on a polystyrene column on an aluminium beam fixed

to the azimuth pedestal of the compact range, which allows the PGM and receive antenna to rotate in azimuth, θ, for a fixed bistatic angle, γ. The principle of reciprocity allows the mounted wideband receive antenna to act as the incident wave where the fixed bistatic angle is equal to the incident angle, $\gamma = \theta_i$. The antenna reflector then acts as the receiver antenna and the varying azimuth angle is then equal to the reflected angle, $\theta = \theta_r$.

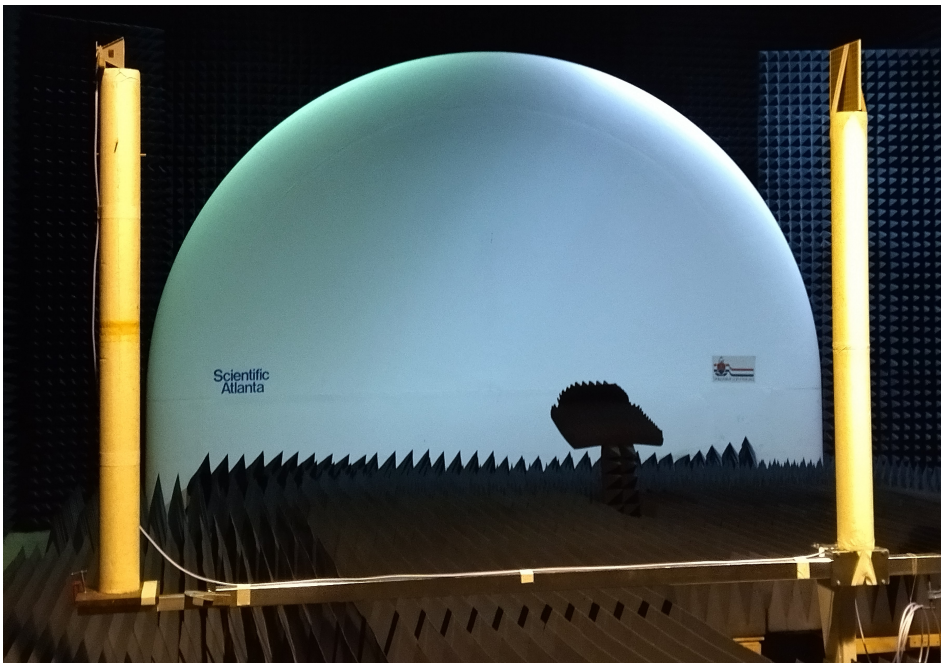

Figure 4.8. Bistatic measurement setup of the compact range.

The finite separation (3 m) between the PGM and the receiver antenna must be larger than the far-field target to receiver distance. This distance is calculated with,

$$R \geq \frac{2D^2}{\lambda}, \tag{4.1}$$

as 2.76 m for the manufactured PGM (0.288 m $\times$ 0.288 m) which was designed to operate at 5 GHz. The receiver antenna was a 2-18 GHz AEL double ridged guide horn antenna. The coupling between the receiver and incident plane wave was eliminated using time gating during the measurements. The calibration was performed with a conducting sphere with a diameter of 153 mm.

4.4.2 Bistatic measurement results

A bistatic measurement was performed on the prototype PGM with $\gamma = -30^\circ$ while varying θ. For this setup the incident wave direction (θ_i) is equivalent to γ and the reflected wave direction (θ_r) equal to the varying θ. The simulated and measured results are shown in Figure 4.9. For an incident angle of $\theta_i = \gamma = -30^\circ$ a reflected wave peak was observed at approximately $\theta_r = -48^\circ$.

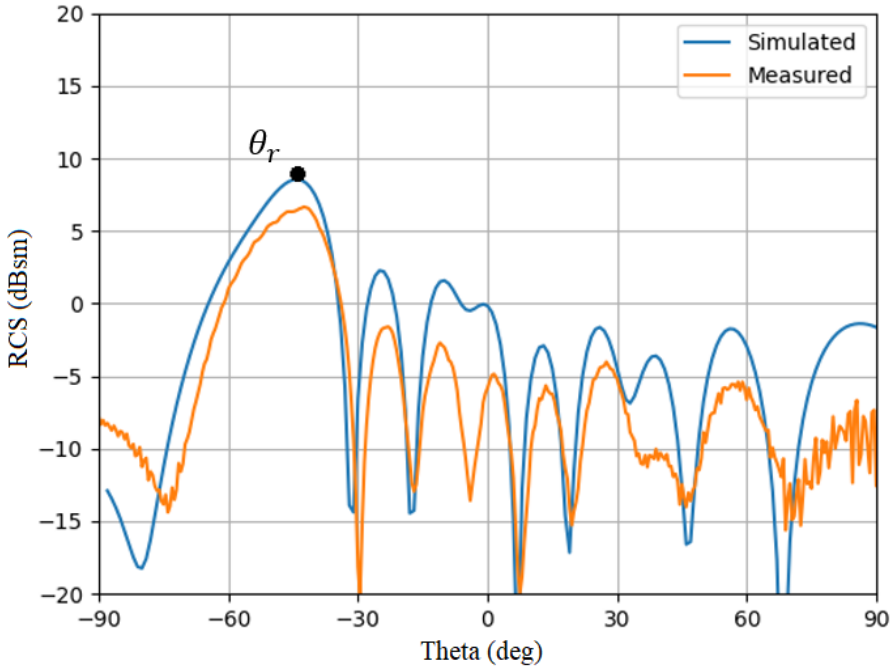

Figure 4.9. Bistatic measurement (VV polarisation) and simulation result for an incident angle of $\theta_i = \gamma = -30^\circ$.

This PGM was designed with a phase gradient in only one direction, the x-axis ($\nabla\phi_y = 0$). The incident angle, (θ_i, φ_i), was varied only in the θ direction, with constant $\varphi_i = 0^\circ$. The parameters of the manufactured PGM's AMC elements are given in Table 4.1. The values of the symbols required to predict the directions of the reflected wave are given in Table 4.2.

The measured result corresponds very well with the simulated result as shown in Figure 4.9. The proposed method of reflected wave direction was then used with an incident wave direction of $\theta_i = -30^\circ$ to calculated the predicted reflected waves. Three active diffraction order modes are predicted as $\eta_G = [-1, 0, 1]$. The reflected wave directions predicted for these active diffraction order modes are calculated as $\theta_{r_1} = -48.59^\circ$, $\theta_{r_2} = -7.18^\circ$ and $\theta_{r_3} = 30^\circ$.

A clear discrepancy is observed between the predicted and measured/simulated results. Only a single reflected wave direction, $\theta_r = -48^\circ$, is observed in the measured/simulated results, but three active diffraction order modes are calculated which in turn is expected to produce three reflected wave directions. The predicted waves for diffraction orders of $\eta_G = -1$, ($\theta_r = 30^\circ$), and $\eta_G = 0$, ($\theta_r = -7^\circ$), are not observed in the measured/simulated results shown in Figure 4.9. A possible explanation of the discrepancy could be the size of the PGM being too small. The size of the PGM was restricted due to the far-field limitation (3 m) selected, based on the practical size of the CATR.

4.4.3 Investigate discrepancy between predicted and measured/simulated results

To investigate the missing predicted reflected waves the metasurface was reconfigured from a 3×3 subcell configuration as shown in Figure 4.1 to a 2×6 configuration as shown in Figure 4.10. This alternative configuration adds three additional subcell periods to the measurement plane of interest in which the gradient operates and the incident and reflected wave directions occur. The PGM consists of the same design parameters as discussed in Section 3.5.3 with the major difference being the layout of the subcells. This surface consisting of 2×6 subcells was simulated instead of the 3×3 subcell arrangement. The simulated scattering from this metasurface is shown in Figures 4.11 and 4.12. Three distinct reflected waves are observed at $\theta_{r_1} = -48^\circ$, $\theta_{r_2} = -7^\circ$ and $\theta_{r3} = 30^\circ$ which correspond very well with the three predicted waves. This simulation shows that the manufactured PGM measured in the CATR contained too few subcell periods which lead to two of the three reflected wave directions not being

observed. If the CATR allowed for a larger PGM with more subcell periods to be measured the three predicted reflected wave directions would be observed in the measured results, as shown in the simulated results of such a larger PGM in Figures 4.11 and 4.12.

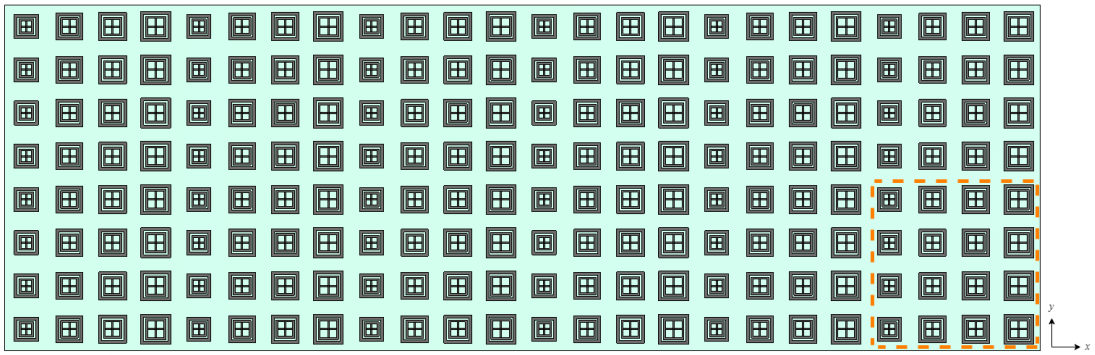

Figure 4.10. The front view of the 2×6 PGM arrangement using AMC elements described by Table 3.2. The dashed line indicates a subcell of 4×4 AMC elements.

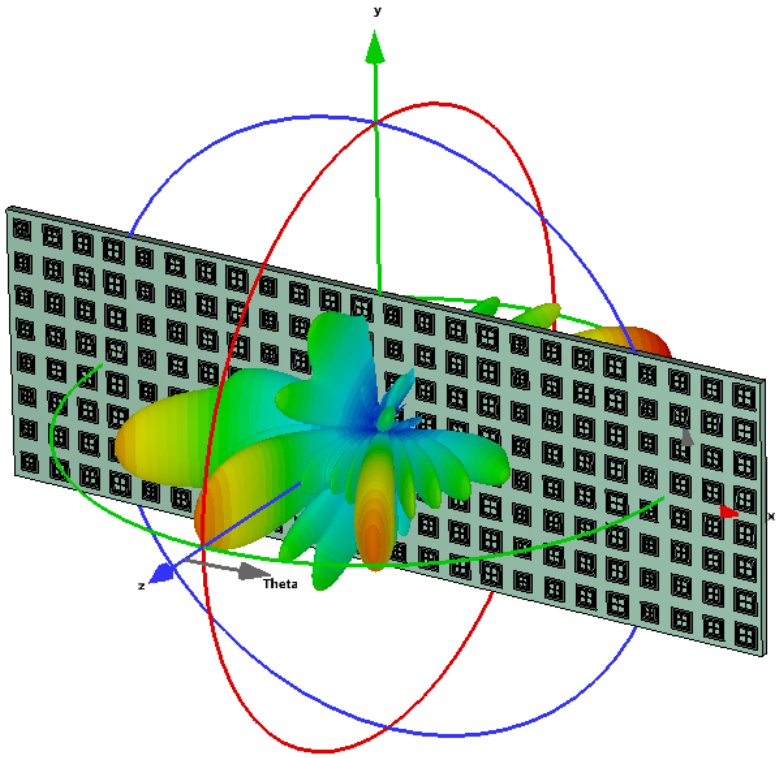

Figure 4.11. 3-D scattering pattern for incident plane wave at $\theta_i = 30°$, $\varphi_i = 180°$ for 2×6 PGM.

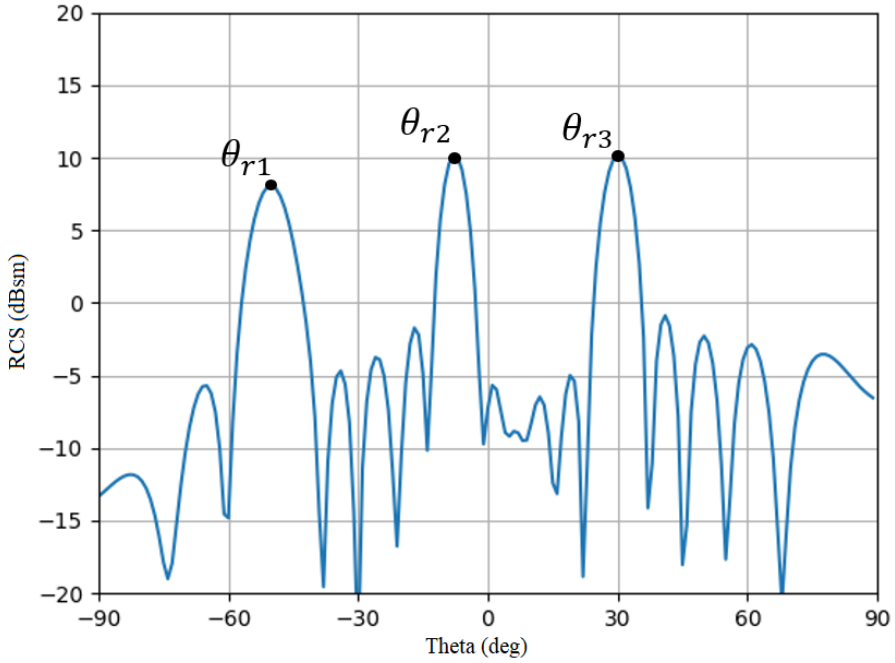

Figure 4.12. Bistatic simulation result for an incident angle of $\theta_i = \gamma = -30°$ for 2×6 PGM. Three peaks are observed at $\theta_{r_1} = -48°$, $\theta_{r_2} = -7°$ and $\theta_{r3} = 30°$.

The comparison between the predicted, simulated and measured reflected wave directions are summarised in Table 4.6.

Table 4.6. Summary of predicted, simulated and measured reflected wave directions for the bistatic PGM measurement.

	Theoretical (Predicted)		**2×6 PGM (Simulated)**		**3×3 PGM (Measured)**	
η_G	θ_r	φ_r	θ_r	φ_r	θ_r	φ_r
-1	30°	0°	30°	0°	-	-
0	7.18°	180°	7°	180°	-	-
1	48.59°	180°	48°	180°	48°	180°

4.5 SUMMARY

This chapter presented various measured and simulated results. The reflected wave directions from the measured and simulated results are compared to the prediction method proposed in this study.

The manufactured PGM described in Section 4.2 was measured in the CATR. For the monostatic setup the measurements agreed well with the simulated results. A peak on the monostatic result indicates that the incident wave direction is equal to the reflected wave direction. This limitation meant that not all the active diffraction order modes could be observed for an incident angle. For each incident wave direction, all reflected wave directions were calculated. For each incident peak there were multiple reflected wave directions predicted. The prediction method estimated a reflected wave direction equal to the incident wave direction for each of the observed reflected peaks. The measured results also corresponded very well with the simulated results.

Bistatic measurements were conducted and compared with simulation results as well as the predicted reflected wave directions. The measurement results corresponded very well with the simulated results. However, three reflected wave directions were predicted using the proposed method. To investigate the impact of the PGM size on the simulated results the initial 3×3 PGM was rearranged to a 2×6 PGM to increase the periodicity on the phase gradient axis. The simulation of the 2×6 PGM clearly showed the three predicted reflected waves. These simulated reflected wave directions corresponded very well with the three predicted reflected wave directions.

CHAPTER 5 CONCLUSION

5.1 CONCLUSION

The main objective of this study was to extend the generalised Snell's law of reflection to incorporate diffraction order elements for incident angles from arbitrary directions. Additionally this extended method needed to account for phase gradients in multiple directions. A method was required to predict additional reflected energy close to the plane of the PGM not predicted by the extended Snell's law of reflection. Finally the method of prediction needed to be compared to simulations and measurements of a manufactured PGM.

The first objective of this study was to extend the work of [15] and [19] to allow for an incident wave from an arbitrary angle. The wave vector dependent Snell's law formulated in (2.6) was extended by defining an equation for each axis to allow an arbitrary incident angle, (θ_i, φ_i). The reflected wave direction can then be calculated by simultaneously solving these two equations.

A planar PGM with phase gradients in the two in-plane directions, will introduce two additional wave vectors to the reflected wave vector. When the angle of incidence is small or close to the normal vector, the magnitude of the reflected wave vector is smaller than that of the incident wave vector. The direction of the anomalously reflected wave can be determined from the incident wave vector components and additional phase gradient components. With the addition of the diffraction order elements to the generalised Snell's law of reflection, the

direction of the reflected waves from a PGM, for scenarios where the incident angle exceeds the critical value, can be predicted as real values as opposed to complex values.

The second objective was to extend this method further to account for phase gradients in two orthogonal in-plane directions of the PGM. By simply defining a phase gradient for the x- and y-direction and substituting these into the previously extended formulas this objective was achieved. This modified generalised Snell's law accounts for PGMs with different phase gradients in two orthogonal in-plane directions. This extended formulation also predicts a reflected wave direction for each valid diffraction order.

The third objective of this study was to utilise array theory to account for the finite nature of PGMs to estimate the additional reflected energy observed close to the plane of the PGM as shown in [16]. The scattering from a PGM was analysed as an equally spaced uniformly excited planar array. This scattering from a PGM was incorporated into the array theory formulas by equating the phase difference from array theory to the phase gradient of the PGM; the specular reflected angle from array theory to the incident angle of the PGM; and also incorporating the diffraction order mode as part of the phase difference as was done during the extended Snell's law derivation. The visible space region for each diffraction order mode can then be plotted on the normalised array factor plot to show the location (direction) of the scattered energy as shown in Figure 3.2. This method of prediction allows the estimation of any scattered energy in a visible space region, not just when an array factor peak falls within the visible space region as is the case with the Snell's law prediction methods.

The fourth and last objective was to design, simulate and measure various PGMs which were used to compare the reflected wave directions with the predicted wave directions. A PGM was designed and simulated in CST Studio Suite [21] to operate at 10 GHz and used for extensive verification of the proposed prediction method. A second PGM designed at 5 GHz was manufacture and measured in the CATR. Monostatic RCS results were compared with simulations as well as with the proposed prediction method. The conventional setup of a CATR was also adapted to perform bistatic RCS measurements of the PGM for different scattering angles. The proposed method for the estimation of the reflected wave directions

from a PGM in this study was successfully verified using numerous simulated and measured results.

5.2 FUTURE WORK

The method proposed in this study is only able to predict the reflected wave directions. In [48] a general method was proposed to control the diffraction pattern both in angle and energy ratio between the scattered beams. This proposed method does however not account for scattered beams which peaks would fall outside but close to the plane of the PGM. Further investigation can be conducted on how, using array theory, the method proposed in [48] can be extended to also account for these scattered beams that fall outside but close to the plane of the PGM.

Another interesting topic for future work would be to utilise the proposed method to improve the RCS manipulation of complex objects. A good starting point could be to investigate the RCS reduction improvement of a dihedral corner reflector when using this method of prediction to design PGMs that achieve this goal.

REFERENCES

[1] C. A. Balanis, *Antenna Theory: Analysis and Design*, 3rd ed. New York: Wiley, 2005.

[2] M. E. de Cos, Y. Alvarez-Lopez, and F. L. H. Andres, "A novel approach for RCS reduction using a combination of artificial magnetic conductors," *Progress In Electromagnetics Research*, vol. 107, pp. 147–159, 2010.

[3] M. Paquay, J.-C. Iriarte, I. Ederra, R. Gonzalo, and P. de Maagt, "Thin AMC structure for radar cross-section reduction," *IEEE Transactions on Antennas and Propagation*, vol. 55, no. 12, pp. 3630–3638, 2007.

[4] W. W. Salisbury, "Absorbent Body for Electromagnetic Waves," U.S. Patent 2 599 944, Jun. 10, 1952.

[5] Q. Gao, Y. Yin, D.-B. Yan, and N.-C. Yuan, "Application of metamaterials to ultra-thin radar-absorbing material design," *Electronics Letters*, vol. 41, no. 17, pp. 936–937, 2005.

[6] N. I. Landy, S. Sajuyigbe, J. J. Mock, D. R. Smith, and W. J. Padilla, "Perfect metamaterial absorber," *Physical Review Letters*, vol. 100, no. 20, p. 207402, 2008.

[7] W. Chen, C. A. Balanis, and C. R. Birtcher, "Checkerboard EBG surfaces for wideband radar cross section reduction," *IEEE Transactions on Antennas and Propagation*, vol. 63,

no. 6, pp. 2636–2645, 2015.

[8] C. A. Balanis, M. A. Amiri, A. Y. Modi, S. Pandi, and C. R. Birtcher, "Applications of AMC-based impedance surfaces," *EPJ Applied Metamaterials*, vol. 5, p. 3, 2018.

[9] A. Y. Modi, M. A. Alyahya, C. A. Balanis, and C. R. Birtcher, "Metasurface-based method for broadband RCS reduction of dihedral corner reflectors with multiple bounces," *IEEE Transactions on Antennas and Propagation*, vol. 68, no. 3, pp. 1436–1447, 2020.

[10] W. Zhang, Y. Liu, S. Gong, J. Wang, and Y. Jiang, "Wideband RCS reduction of a slot array antenna using phase gradient metasurface," *IEEE Antennas and Wireless Propagation Letters*, vol. 17, no. 12, pp. 2193–2197, 2018.

[11] F. Yuan, G.-M. Wang, H.-X. Xu, T. Cai, X.-J. Zou, and Z.-H. Pang, "Broadband RCS reduction based on spiral-coded metasurface," *IEEE Antennas and Wireless Propagation Letters*, vol. 16, pp. 3188–3191, 2017.

[12] Y. Li, J. Zhang, S. Qu, J. Wang, H. Chen, Z. Xu, and A. Zhang, "Wideband radar cross section reduction using two-dimensional phase gradient metasurfaces," *Applied Physics Letters*, vol. 104, no. 22, p. 221110, 2014.

[13] S. Sun, Q. He, S. Xiao, Q. Xu, X. Li, and L. Zhou, "Gradient-index meta-surfaces as a bridge linking propagating waves and surface waves," *Nature Materials*, vol. 11, no. 5, pp. 426–431, 2012.

[14] N. Yu, P. Genevet, M. A. Kats, F. Aieta, J.-P. Tetienne, F. Capasso, and Z. Gaburro, "Light propagation with phase discontinuities: generalized laws of reflection and refraction," *Science*, vol. 334, no. 6054, pp. 333–337, 2011.

[15] Y. Xie, W. Wang, H. Chen, A. Konneker, B.-I. Popa, and S. A. Cummer, "Wavefront modulation and subwavelength diffractive acoustics with an acoustic metasurface,"

Nature Communications, vol. 5, no. 1, pp. 1–5, 2014.

[16] W. Barnard, J. W. Odendaal, and J. Joubert, "Predicting the direction of the reflected wave from a phase gradient metasurface with arbitrary incident angle," presented at the *2021 IEEE International Symposium on Antennas and Propagation and USNC-URSI Radio Science Meeting*, Singapore, Dec. 2-10, 2021.

[17] A. Y. Modi, C. A. Balanis, and C. Birtcher, "AMC cells for broadband RCS reduction checkerboard surfaces," in *2017 IEEE International Symposium on Antennas and Propagation USNC/URSI National Radio Science Meeting*, 2017, pp. 1915–1916.

[18] J. C. Iriarte Galarregui, A. Tellechea Pereda, J. L. M. de Falcón, I. Ederra, R. Gonzalo, and P. de Maagt, "Broadband radar cross-section reduction using AMC technology," *IEEE Transactions on Antennas and Propagation*, vol. 61, no. 12, pp. 6136–6143, 2013.

[19] X. Ding, C. Guan, Z. Wang, S. Liu, K. Zhang, X. Gu, Q. Wu, and M. Jin, "Metasurface for bending the reflected wave under oblique incidence," *IEEE Transactions on Magnetics*, vol. 55, no. 11, pp. 1–4, 2019.

[20] A. Y. Modi, C. A. Balanis, and C. Birtcher, "Refinement and unification of checkerboard and gradient index RCS-reduction metasurfaces," in *2018 IEEE International Symposium on Antennas and Propagation USNC/URSI National Radio Science Meeting*, 2018, pp. 2287–2288.

[21] *CST Studio Suite Electromagnetic Field Simulation Software*, Dassault Systèmes, 2021.

[22] Y. Zhao, C. Yu, J. Gao, X. Yao, T. Liu, W. Li, and S. Li, "Broadband metamaterial surface for antenna RCS reduction and gain enhancement," *IEEE Transactions on Antennas and Propagation*, 2015.

[23] D. Sievenpiper, L. Zhang, R. Broas, N. Alexopolous, and E. Yablonovitch, "High-impedance electromagnetic surfaces with a forbidden frequency band," *IEEE Transactions on Microwave Theory and Techniques*, vol. 47, no. 11, pp. 2059–2074, 1999.

[24] B. Lin, J. Guo, L. Lv, Z. Liu, X. Ji, and J. Wu, "An ultra-wideband reflective phase gradient metasurface using pancharatnam-berry phase," *IEEE Access*, vol. 7, pp. 13 317–13 325, 2019.

[25] A. Tellechea, J. C. Iriarte, I. Ederra, and R. Gonzalo, "Planar EBG technology chessboard configuration to reduce RCS in W band," in *2013 7th European Conference on Antennas and Propagation (EuCAP)*, 2013, pp. 3935–3938.

[26] W. Chen, C. A. Balanis, and C. R. Birtcher, "Dual wide-band checkerboard surfaces for radar cross section reduction," *IEEE Transactions on Antennas and Propagation*, vol. 64, no. 9, pp. 4133–4138, 2016.

[27] W. Chen, C. A. Balanis, and C. Birtcher, "Dual frequency band RCS reduction using checkerboard designs," in *2017 IEEE International Symposium on Antennas and Propagation & USNC/URSI National Radio Science Meeting*, 2017, pp. 1913–1914.

[28] Y. Zhao, X. Cao, J. Gao, X. Yao, T. Liu, W. Li, and S. Li, "Broadband low-RCS metasurface and its application on antenna," *IEEE Transactions on Antennas and Propagation*, vol. 64, no. 7, pp. 2954–2962, 2016.

[29] Z. Zheng, Z. Li, and J. Su, "An optimal-arranged metasurface for wideband RCS reduction," in *2015 IEEE 6th International Symposium on Microwave, Antenna, Propagation, and EMC Technologies (MAPE)*, 2015, pp. 525–527.

[30] T. Han, X. Cao, J. Gao, and Y. Zhao, "Broadband and wide-angle RCS reduction based on an optimal-arranged metasurface," in *2017 Sixth Asia-Pacific Conference on Antennas and Propagation (APCAP)*, 2017, pp. 1–3.

[31] B. Sima, K. Chen, and Y. Feng, "Reflective 1-bit coding metasurface for frequency selective RCS reduction," in *2018 IEEE Asia-Pacific Conference on Antennas and Propagation (APCAP)*, 2018, pp. 519–520.

[32] T. J. Cui, M. Q. Qi, X. Wan, J. Zhao, and Q. Cheng, "Coding metamaterials, digital metamaterials and programmable metamaterials," *Light: Science & Applications*, vol. 3, no. 10, p. e218, 2014.

[33] D. Sang, Q. Chen, L. Ding, M. Guo, and Y. Fu, "Design of checkerboard AMC structure for wideband RCS reduction," *IEEE Transactions on Antennas and Propagation*, vol. 67, no. 4, pp. 2604–2612, 2019.

[34] Y. Wang, K. Chen, Y. Li, and Q. Cao, "Design of nonresonant metasurfaces for broadband rcs reduction," *IEEE Antennas and Wireless Propagation Letters*, vol. 20, no. 3, pp. 346–350, 2021.

[35] A. Y. Modi, C. A. Balanis, C. R. Birtcher, and H. N. Shaman, "Novel design of ultrabroadband radar cross section reduction surfaces using artificial magnetic conductors," *IEEE Transactions on Antennas and Propagation*, vol. 65, no. 10, pp. 5406–5417, 2017.

[36] W. Chen, C. A. Balanis, C. R. Birtcher, and A. Y. Modi, "Cylindrically curved checkerboard surfaces for radar cross-section reduction," *IEEE Antennas and Wireless Propagation Letters*, vol. 17, no. 2, pp. 343–346, 2018.

[37] W. L. Stutzman and G. A. Thiele, "Array Antennas," in *Antenna Theory and Design*, 3rd ed. Hoboken, NJ, USA: Wiley, 2012, pp. 275–280.

[38] V. Ajaikumar, K. Jose, P. Mohanan, and K. Nair, "Reduction of radar cross section of corner reflectors using strip grating technique," in *IEEE Antennas and Propagation Society International Symposium*, 1992, pp. 707–710.

[39] L. Li, H. Shi, W. Li, J. Li, A. Zhang, and W. Li, "Main beam angle control microstrip antenna based on phase gradient metasurface," in *2016 11th International Symposium on Antennas, Propagation and EM Theory (ISAPE)*, 2016, pp. 1–4.

[40] W. Zhang, Y. Liu, and S. Gong, "Wideband RCS reduction using two dimensional phase gradient metasurface," in *2017 Sixth Asia-Pacific Conference on Antennas and Propagation (APCAP)*, 2017, pp. 1–3.

[41] Y. Zhou, G. Zhang, P. Zhou, H. Chen, J. Xie, and L. Deng, "A microwave RCS reduction structure by antarafacial reflection design of gradient metasurface," in *2016 Progress in Electromagnetic Research Symposium (PIERS)*, 2016, pp. 4126–4130.

[42] X. Luo, Q. Zhang, and Y. Zhuang, "Tai-chi-inspired pancharatnam-berry phase metasurface for dual-band RCS reduction," in *2017 IEEE International Symposium on Antennas and Propagation & USNC/URSI National Radio Science Meeting*, 2017, pp. 83–84.

[43] L. Zhu, J. Sun, Q. Cao, and H. Li, "Research on in-band stealth of antenna based on phase gradient metasurface," *Microwave and Optical Technology Letters*, vol. 64, no. 5, pp. 939–945, 2022.

[44] Y. Liu and Y. Song, "Wideband rcs reduction based on reflective phase gradient metasurface," in *2022 International Conference on Optoelectronic Information and Functional Materials (OIFM 2022)*, vol. 12255. SPIE, 2022, pp. 162–166.

[45] T. Zhang, X. Pang, H. Zhang, and Q. Zheng, "Ultra-broadband rcs reduction and gain enhancement of patch antennas by phase gradient metasurfaces," *IEEE Antennas and Wireless Propagation Letters*, 2022.

[46] K. Singh, M. U. Afzal, A. Lalbakhsh, and K. P. Esselle, "Reflecting phase-gradient metasurface for radar cross section reduction," in *2021 IEEE Asia-Pacific Microwave Conference (APMC)*. IEEE, 2021, pp. 344–346.

[47] Y. Fan, J. Wang, X. Fu, Y. Li, Y. Pang, L. Zheng, M. Yan, J. Zhang, and S. Qu, "Recent developments of metamaterials/metasurfaces for RCS reduction," *EPJ Applied Metamaterials*, vol. 6, p. 15, 2019.

[48] Y. Wang, Y. Yuan, G. Yang, X. Ding, Q. Wu, Y. Jiang, S. N. Burokur, and K. Zhang, "Perfect control of diffraction patterns with phase-gradient metasurfaces," *ACS Applied Materials & Interfaces*, vol. 14, no. 14, pp. 16 856–16 865, 2022.

[49] Y. Liu, K. Li, Y. Jia, Y. Hao, S. Gong, and Y. J. Guo, "Wideband RCS reduction of a slot array antenna using polarization conversion metasurfaces," *IEEE Transactions on Antennas and Propagation*, vol. 64, no. 1, pp. 326–331, 2016.

[50] F. T. Ulaby, E. Michielssen, and U. Ravaioli, *Fundamentals of Applied Electromagnetics*. Pearson Upper Saddle River, NJ, 2015, vol. 7.

[51] J. Joubert, J. Vardaxoglou, W. G. Whittow, and J. W. Odendaal, "CPW-fed cavity-backed slot radiator loaded with an AMC reflector," *IEEE Transactions on Antennas and Propagation*, vol. 60, no. 2, pp. 735–742, 2011.

[52] Rogers Corporation, "RT/duroid 5870/5880 datasheet," publication #92-101, 2022.

ADDENDUM A DETERMINE GRATING LOBE AND VISIBLE SPACE OVERLAP

A method to determine when the visible space overlaps with at least -3 dB of the grating lobe is provided in this addendum.

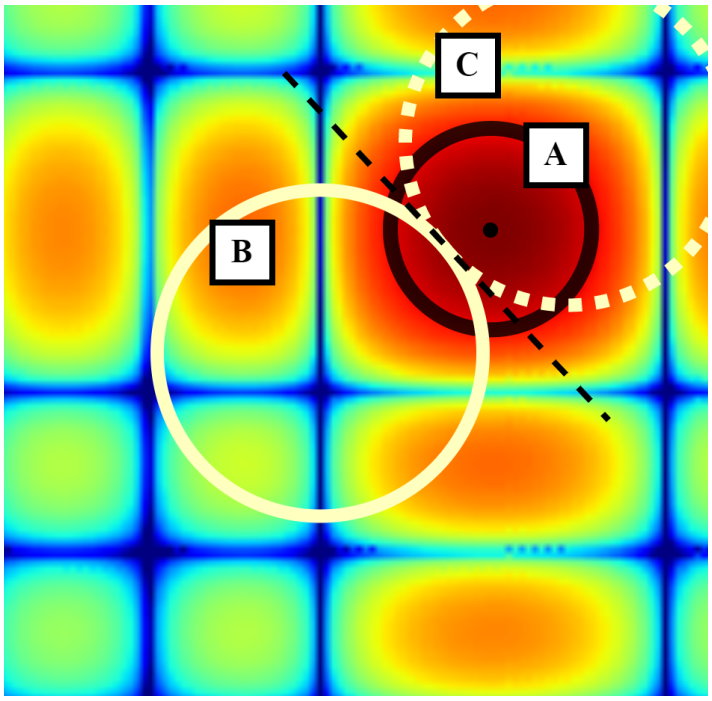

Figure A.1. Illustration of visible space overlapping with at least -3 dB of grating lobe. Label A shows the -3 dB ellipse of the grating lobe. Label B shows the visible space ellipse. Label C shows the shifted visible space ellipse.

In Figure A.1 a portion of the normalised array factor, shown in Figure 3.2, is shown with three regions indicated by labels A, B and C. Region A shows the -3 dB ellipse of the normalised array factor or grating lobe, with the peak also indicated by a dot. Region B is the visible space ellipse which is overlapping with the -3 dB ellipse of the array factor, but not overlapping the peak of the array factor. Region C shows the mirrored visible space towards the peak of the array factor.

As the peak of the array factor is not within the visible space (region B) the reflected wave direction calculation will result in an imaginary value for θ_r. One method to determine if at least -3 dB of the array factor overlaps with the visible space region includes mirroring the visible space region towards the array factor peak, ie. shifting the visible space (B) towards the array factor peak by two times the radius of the ellipse in the peak direction. This is shown in Figure A.1 by the initial visible space (B) and the shifted visible space (C). The shifted visible space now contains the array factor peak. Then calculating the reflected wave direction, (θ_r, φ_r), for the shifted visible space and determining if the half power beamwidth (HPBW) of this reflected wave falls completely within the shifted visible space region, or if a portion of the HPBW falls outside the shifted visible space region and overlaps with the original unshifted visible space region.

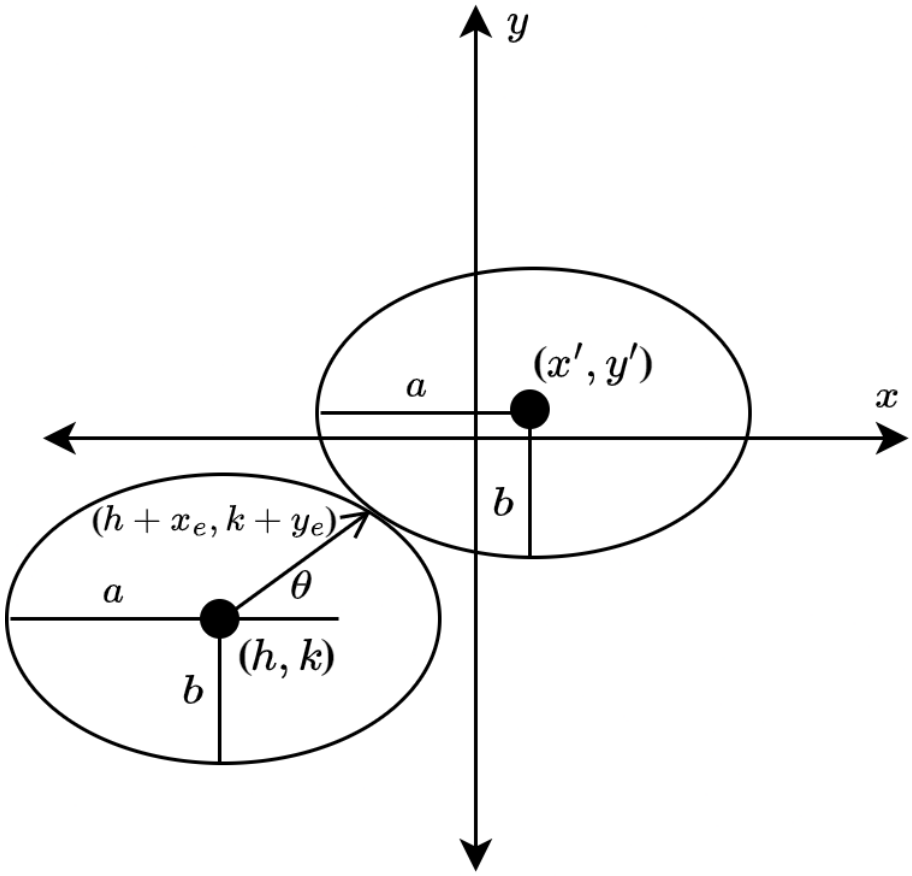

Figure A.2. Illustration of shifting ellipse towards centre of axis by the radius of the ellipse in that direction.

The shifting of an ellipse from centre point (h, k) to a shifted centre point (x', y') is illustrated in Figure A.2. The shifted centre point (x', y') is calculated as twice the distance of the point on the ellipse (x_e, y_e) in the same direction of this point (x_e, y_e). The x and y coordinates of any point on an ellipse centred at the origin is calculated as,

$$x_e = \beta d_x cos\theta \tag{A.1}$$

$$y_e = \beta d_y sin\theta. \tag{A.2}$$

Then the centre of the shifted visible space region is calculated as,

$$x' = h + 2x_e \tag{A.3}$$

$$y' = k + 2y_e, \tag{A.4}$$

where,

$$\theta = \arctan\left(\frac{k}{h}\right) \tag{A.5}$$

$$h = \psi_x(0,0) \tag{A.6}$$

$$k = \psi_y(0,0). \tag{A.7}$$

Once the location of the shifted visible space is calculated the direction of the reflected wave, ($\theta_{r_{shift}}$, $\varphi_{r_{shift}}$), for this region can be calculated. To calculate the direction of the reflected wave for the shifted visible space the terms, (x_e, y_e), is incorporated into (3.2) and (3.3) as,

$$\beta sin\theta_{r_{shift}} cos\varphi_{r_{shift}} = \beta sin\theta_i cos(\varphi_i - \pi) + \sigma\nabla\phi_x(1+\eta_G) - 2x_e \tag{A.8}$$

$$\beta sin\theta_{r_{shift}} sin\varphi_{r_{shift}} = \beta sin\theta_i sin(\varphi_i - \pi) + \sigma\nabla\phi_y(1+\eta_G) - 2y_e. \tag{A.9}$$

After the reflected wave direction of the shifted visible space is calculated the HPBW of the reflected wave can be added to the reflected wave direction to determine if the -3 dB ellipse of the reflected wave is completely contained in the shifted visible space, meaning that there is no overlap between the -3 dB ellipse of the array factor and the original visible space. If the -3 dB ellipse of the reflected wave is not completely contained within the shifted visible region, it means that there is an overlap of the -3 dB ellipse of the array factor with the original visible space. The ϕ_r direction of the reflected wave for the initial visible space region can be calculated by simultaneously solving (3.2) and (3.3) regardless of the -3 dB overlap validation discussed. Before this value is selected as the direction of the reflected wave energy the overlap between the -3 dB grating lobe region (A) and visible space region

(B) must be verified.The HPBW of the array factor is calculated in [37] as,

$$HPBW = \frac{2 \times 2\pi}{N}. \tag{A.10}$$

If the visible space region (B) overlaps with the -3 dB grating lobe region (A) then the diffraction order mode is valid and the calculated ϕ_r can be selected as the direction of the reflected wave energy. This is expressed as,

$$\forall \theta_{r_{shift}} (\theta_{r_{shift}} + \frac{HPBW}{2} > 90^{\circ}) \Longrightarrow \phi_r. \tag{A.11}$$

ADDENDUM B ADDITIONAL SIMULATION RESULTS AND CALCULATIONS

Additional simulations were conducted for a multitude of scenarios on the PGM presented in Section 3.5.3. These additional simulations were used to rigorously compare the prediction method presented in this study. The simulation results and additional relevant information is presented in this addendum and summarised in Section 3.6.3 and Table 3.6.

B.1 INCIDENT ANGLE

B.1.1 $\theta_i = 30.6°$, $\varphi_i = 22.4°$

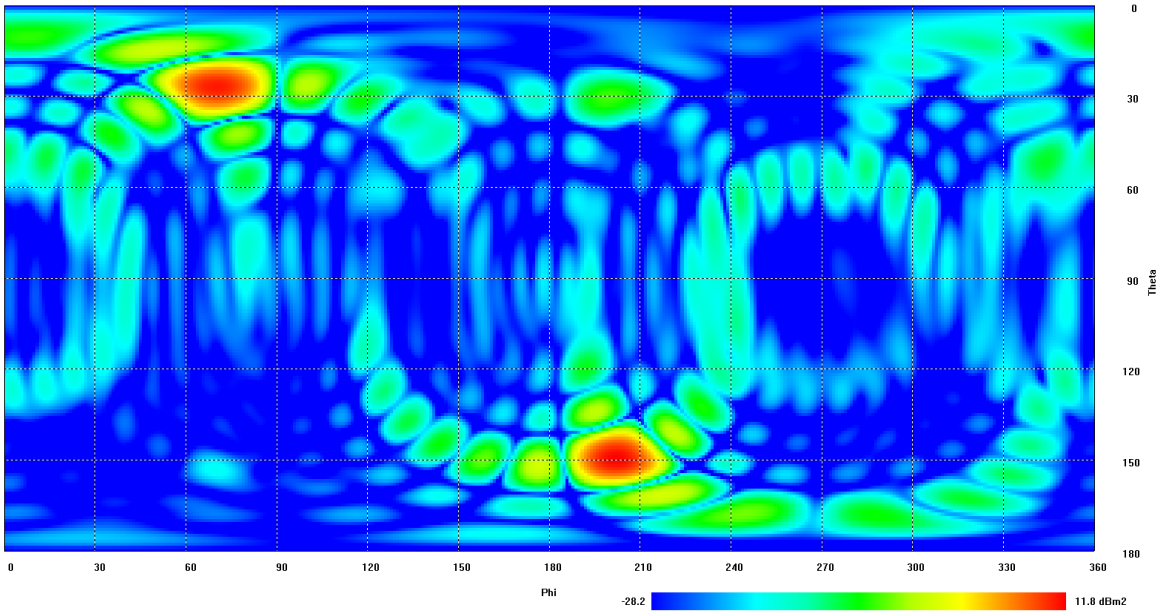

Figure B.1. The bistatic scattering from the PGM with $\theta_i = 30.6°$, $\varphi_i = 22.4°$.

B.1.2 $\theta_i = 40°$, $\varphi_i = 45°$

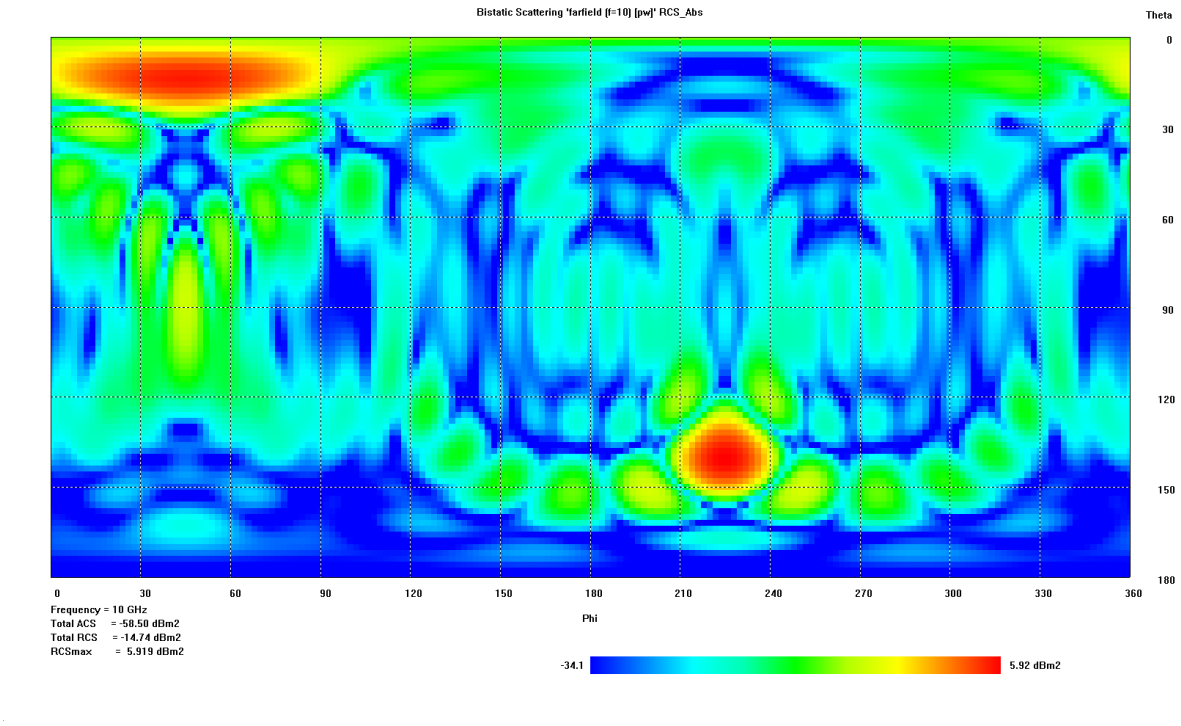

Figure B.2. The bistatic scattering from the PGM with $\theta_i = 40°$, $\varphi_i = 45°$.

The valid diffraction order of $\eta_G = -3$ was not calculated with Snell's law, but the visible space showed significant overlap with the HPBW of the array factor peak. The visible space region is shown in Figure B.3.

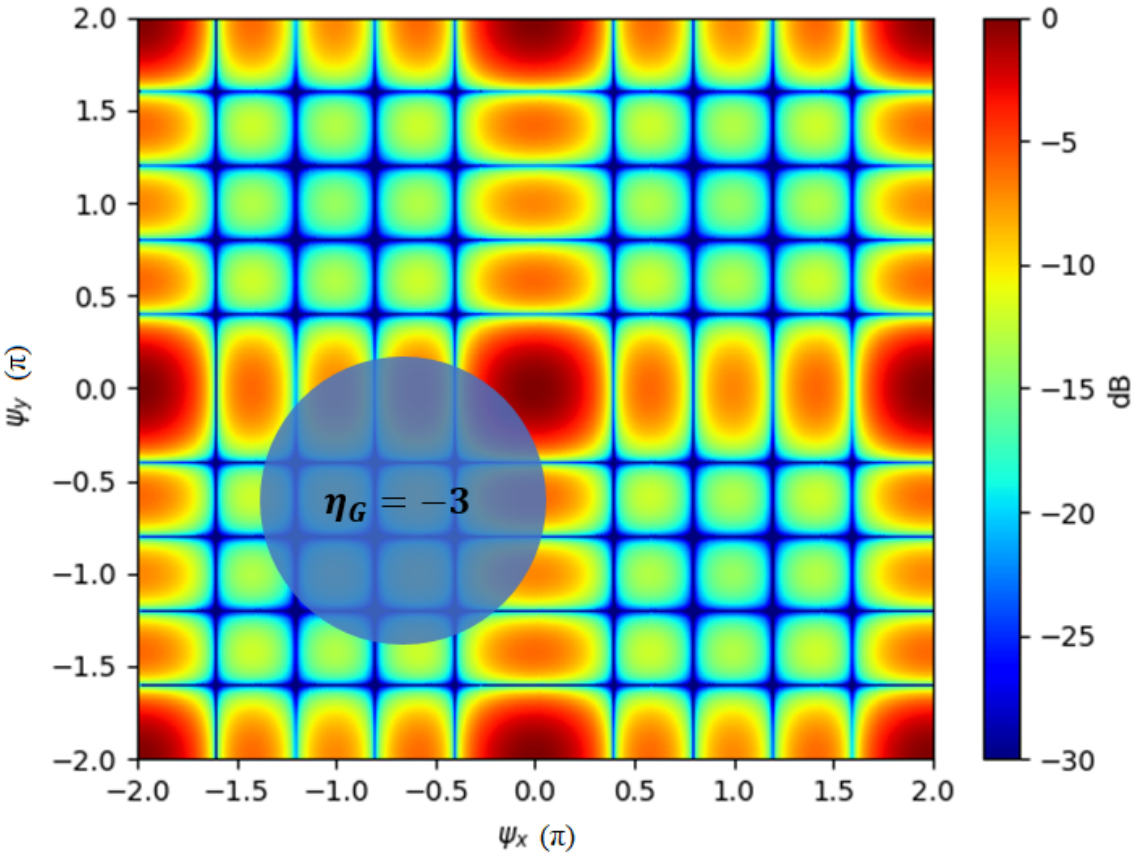

Figure B.3. Visible space region for diffraction order, $\eta_G = -3$ indicated on array factor plot.

B.1.3 $\theta_i = 70°$, $\varphi_i = 135°$

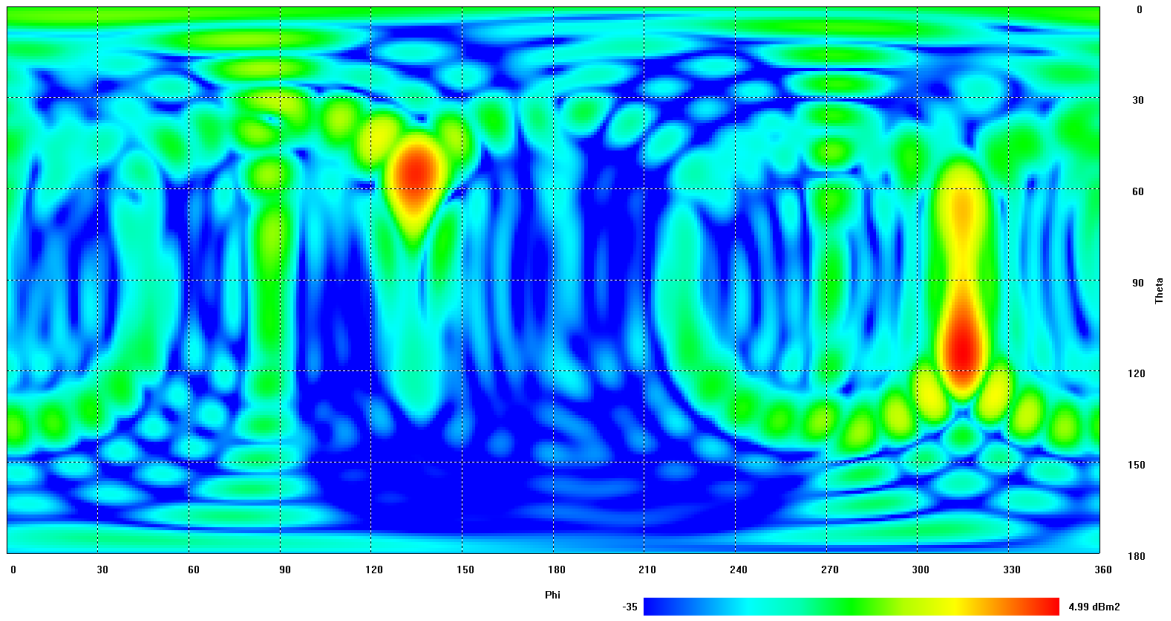

Figure B.4. The bistatic scattering from the PGM with $\theta_i = 70°$, $\varphi_i = 135°$.

The valid diffraction order of $\eta_G = -3$ was calculated with (3.10) and (3.11) with the array factor peak of $\psi_x = -2\pi$ and $\psi_y = 0$. The visible space region is shown in Figure B.5 overlapping with the array factor peak at ($\psi_x = -2\pi$, $\psi_y = 0$).

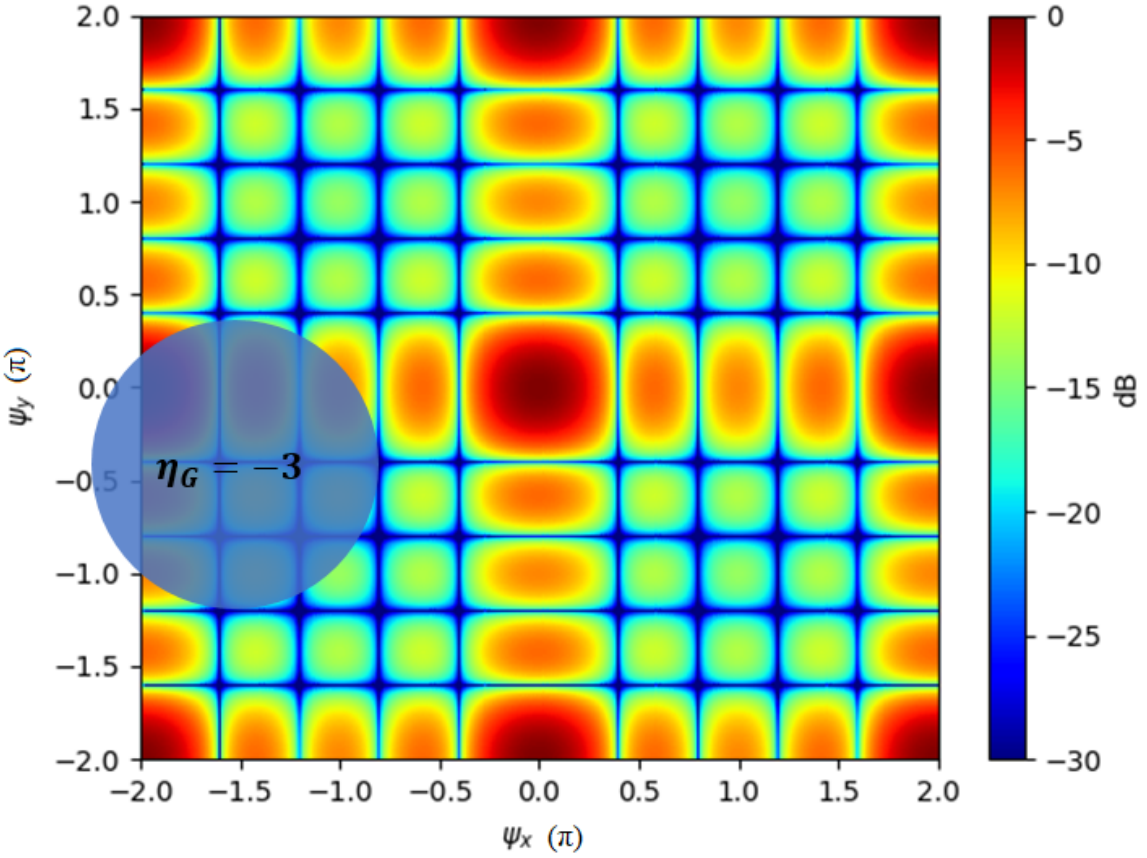

Figure B.5. Visible space region for diffraction order, $\eta_G = -3$ indicated on array factor plot.

B.1.4 $\theta_i = 30°$, $\varphi_i = 160°$

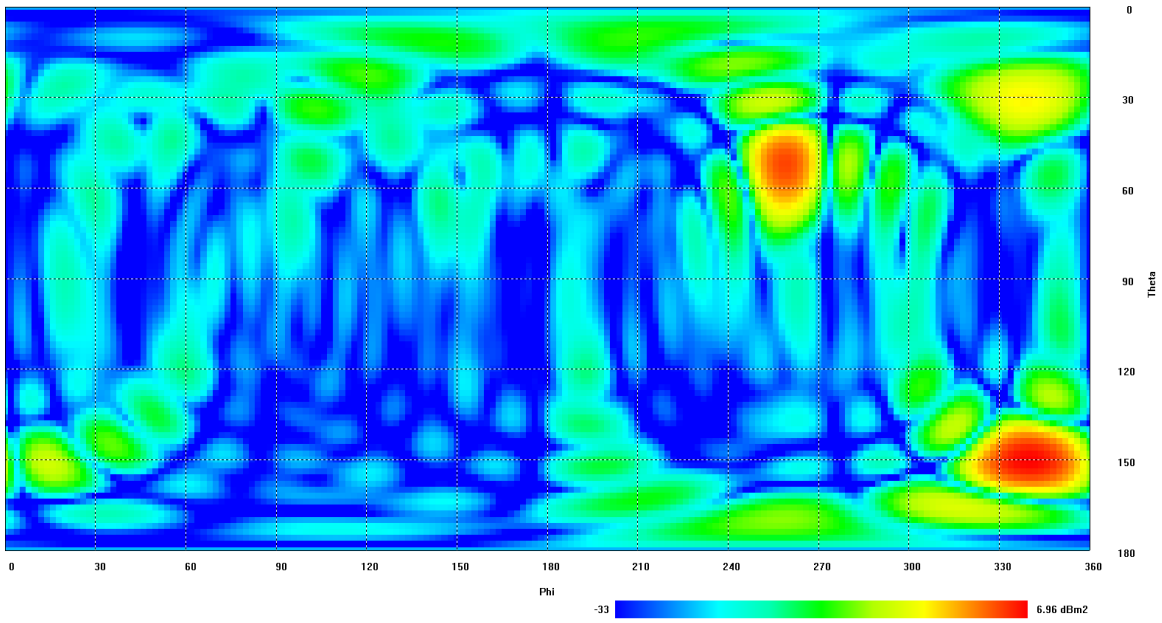

Figure B.6. The bistatic scattering from the PGM with $\theta_i = 30°$, $\varphi_i = 160°$.

B.1.5 $\theta_i = 60°$, $\varphi_i = 200°$

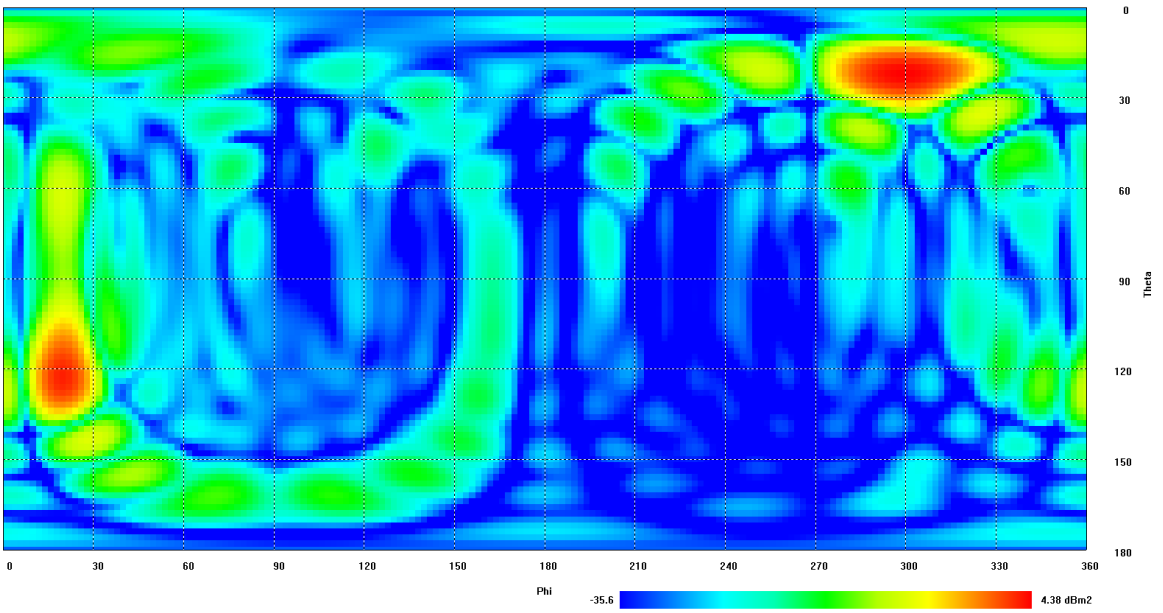

Figure B.7. The bistatic scattering from the PGM with $\theta_i = 60°$, $\varphi_i = 200°$.

B.1.6 $\theta_i = 60°$, $\varphi_i = 340°$

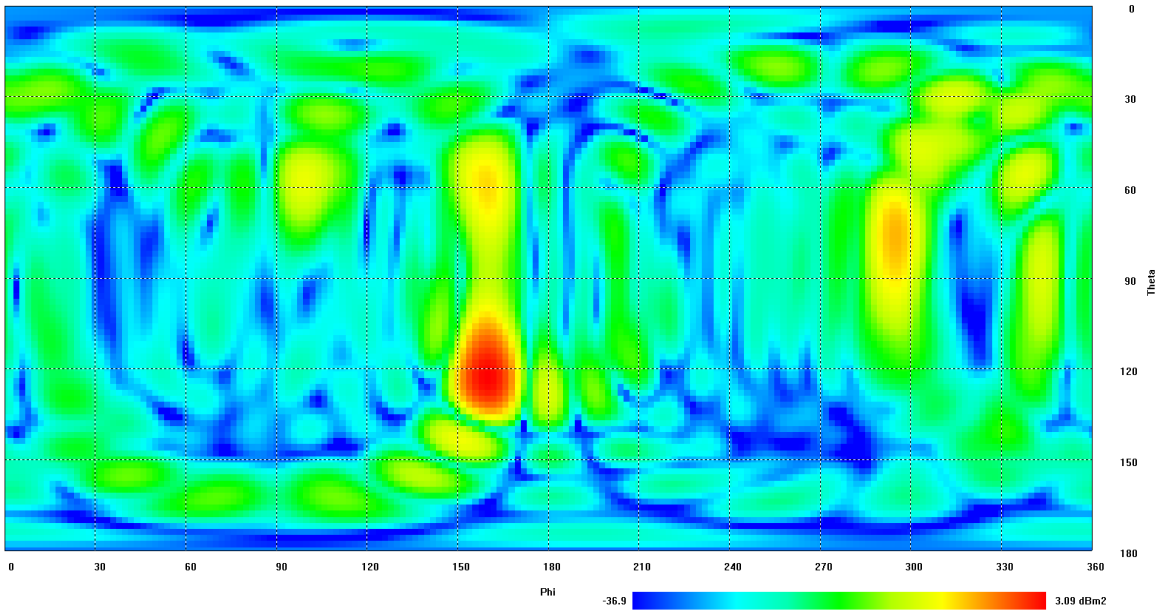

Figure B.8. The bistatic scattering from the PGM with $\theta_i = 60°$, $\varphi_i = 340°$.

The valid diffraction order of $\eta_G = -3$ was not calculated with Snell's law, but the visible space showed significant overlap with the HPBW of the array factor peak at ($\psi_x = 0$, $\psi_y = -2\pi$). The visible space region is shown in Figure B.9.

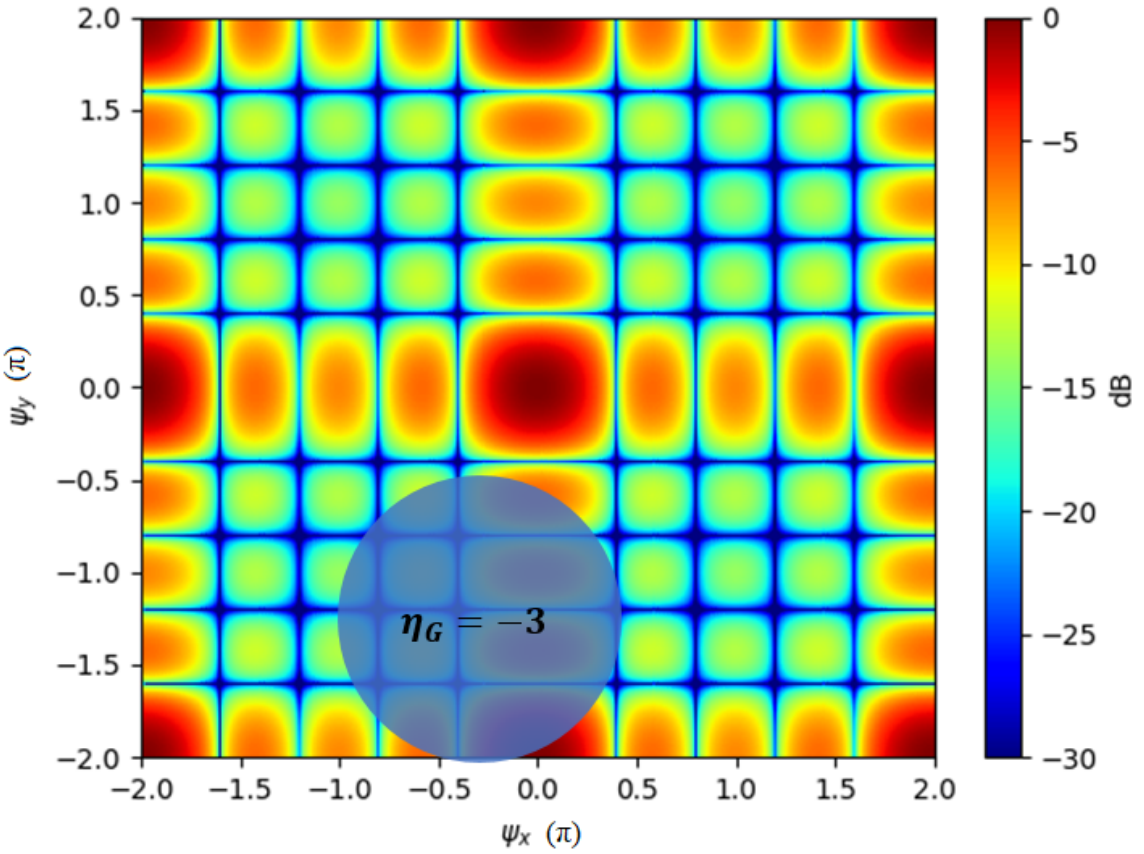

Figure B.9. Visible space region for diffraction order, $\eta_G = -3$ indicated on array factor plot.

ADDENDUM C SOFTWARE

```
import sympy as sym
from sympy import sin, cos
import numpy as np

def snell_extend(theta_0, phi_0, sigma, beta,
                 grad_x, grad_y, diff_x, diff_y):
  theta_r, phi_r = sym.symbols('theta_r phi_r', real=True)
  eq1 = sym.Eq(sin(theta_r)*cos(phi_r),
    sin(theta_0)*cos(phi_0)+(sigma*grad_x/beta)*(1+diff_x))
  eq2 = sym.Eq(sin(theta_r)*sin(phi_r),
    sin(theta_0)*sin(phi_0)+(sigma*grad_y/beta)*(1+diff_y))

  solution = sym.solve((eq1, eq2), (theta_r, phi_r))

  return solution

if __name__ == "__main__":
  theta_in = np.deg2rad(0)#np.deg2rad(60)  #np.deg2rad(30)
  phi_in   = np.deg2rad(180)#np.deg2rad(20)  #np.deg2rad(180)
  theta_0 = theta_in
  phi_0 = phi_in - np.deg2rad(180)

  speed_of_light = 3e8
```

```
frequency = 5e9
wavelength = speed_of_light/frequency
beta = 2*np.pi/wavelength
sigma = 1

period = 0.096
grad_x = -2*np.pi/period
grad_y = 0#-2*np.pi/period

diff_arr = range(-4,4,1)

for diff in diff_arr:
  solutions = wihan_snell_extend( theta_0=theta_0,
    phi_0=phi_0,
        sigma=sigma,
        beta=beta,
        grad_x=grad_x,
        grad_y=grad_y,
        diff_x=diff,
        diff_y=diff)

    if solutions:
      print(f'\ndiffraction order= {diff}')
    else:
      continue

      for sol in solutions:
        theta_r, phi_r = sol
            try:
              print(f'theta_r =
                    {np.rad2deg(float(theta_r.evalf()))},
```

```
        phi_r = {np.rad2deg(float(phi_r.evalf()))}')
    except:
        print(f'theta_r = {theta_r},
        phi_r = {phi_r}')
```